Monitoring loss of tropical forest cover from Sentinel-1 time-series: A CuSum-based approach

Bertrand Ygorra, F. Frappart, Wigneron J.-P., Christophe Moisy, Thibault Catry, F. Baup, E. Hamunyela, S. Riazanoff

International Journal of Applied Earth Observations and Geoinformation 103 (2021) 102532

Contents lists available at ScienceDirect

International Journal of Applied Earth Observations and Geoinformation

journal homepage: www.elsevier.com/locate/jag

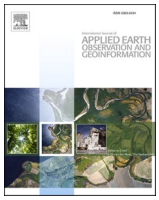

Monitoring loss of tropical forest cover from Sentinel-1 time-series: A CuSum-based approach

B. Ygorra [a,b,c,*], F. Frappart [a,d], J.P. Wigneron [a], C. Moisy [a], T. Catry [e], F. Baup [f], E. Hamunyela [g], S. Riazanoff [b]

[a] INRAE, UMR1391 ISPA, 33140 Villenave d'Ornon, France
[b] VisioTerra, 77420 Champs-sur-Marne, France
[c] Université de Bordeaux, 33400 Talence, France
[d] LEGOS, Université de Toulouse, UMR CNES/CNRS/IRD/UPS, 31400 Toulouse, France
[e] ESPACE-DEV, Univ Montpellier, IRD, Univ Antilles, Univ Guyane, Univ Réunion, Montpellier, France
[f] CESBIO, 31400 Toulouse, France
[g] University of Namibia, Private Bag 13301, Windhoek, Namibia

ARTICLE INFO

Keywords:
Deforestation
Remote sensing
Sentinel-1
Cumulative sum algorithm
Tropical forest
Change detection

ABSTRACT

The forest decline in tropical areas is one of the largest global environmental threats as the growth of both global population and its needs have put an increasing pressure on these ecosystems. Efforts are ongoing to reduce tropical deforestation rates. Earth observations are increasingly used to monitor deforestation over the whole equatorial area. Change detection methods are mainly applied to satellite optical images which face limitations in humid tropical areas. For instance, due to frequent cloud cover in the tropics, there are often long delays in the detection of deforestation events. Recently, detection methods applied to Synthetic Aperture Radar (SAR) have been developed to address the limitations related to cloud cover. In this study, we present an application of a recently developed change detection method for monitoring forest cover loss from SAR time-series data in tropical zone. The method is based on the Cumulative Sum algorithm (CuSum) combined with a bootstrap analysis. The method was applied to time-series of Sentinel-1 ground range detected (GRD) dual polarization (VV, VH) images forming a dataset of 60 images to monitor forest cover loss in a legal forest concession of the Democratic Republic of Congo during the 2018–2020 period. A cross-threshold recombination was then conducted on the computed maps. Evaluated against reference forest cut maps, an overall accuracy up to 91% and a precision up to 75% in forest clear cut detection was obtained. Our results show that more than 60% of forest disturbances were detected before the PlanetScope-based estimated date of cut, which may suggest the capacity of our method to detect forest degradation.

1. Introduction

The tropical forests, which play a critical role in the global climate regulation by recycling ~2.1 Gt CO_2 per year (Federici et al., 2015; Nunes et al., 2020), are being deforested at increasing rates. In Africa, the forest losses in carbon stocks are driven by multiple factors, including legal or illegal selective logging causing degradations, or cuts to fulfil the agricultural needs of local populations (Contreras-Hermosilla et al, 2000). Optical satellite remote sensing is commonly used to monitor forest cover changes (e.g., Global Forest Watch (Bullock et al., 2020; Hansen et al., 2013; Tyukavina et al., 2018)). Yet, the monitoring systems based on this kind of images are likely to provide inaccurate information over regions strongly affected by cloud cover (Hansen et al., 2016). They were also shown to be less robust in regions where forest exhibits strong seasonal variability in the canopy water content (Hamunyela et al., 2017). Studies based on the merging of optical and Synthetic Aperture Radar (SAR) datasets, showed a better temporal accuracy in the detection of forest cuts by accounting for the seasonal changes in the vegetation structure but at the costs of a high computational complexity (Hamunyela et al., 2020). With the advances in the spatial and temporal resolutions of the satellite observations, the application of change detection algorithms to satellite data requires increasing computational platform performances. Some change detection algorithms such as the RADD and JJFAST alerts (Watanabe et al.,

* Corresponding author.
E-mail address: bertrand.ygorra@gmail.com (B. Ygorra).

https://doi.org/10.1016/j.jag.2021.102532
Received 22 April 2021; Received in revised form 30 August 2021; Accepted 30 August 2021
Available online 6 September 2021

2021; FAST, 2021) are currently operational on powerful platforms such as Google Earth Engine, (see Reiche et al., 2021 for instance). As the revisit time of the satellite observations decreases, change detection algorithms based on temporal analysis are increasingly used (Duveiller et al., 2008; Hamunyela et al., 2016; Souza et al., 2013). Among them, a change detection algorithm analysing the temporal stability of the signal through the deviation of a variable to its mean – the cumulative Sum (CuSum) – has been used in environmental studies, including for forest monitoring: (Kucera et al., 2007; Manogaran and Lopez, 2018; Ruiz-Ramos et al., 2020). The CuSum is a change detection method based on statistics to analyse multi-temporal processes, as it allows the detection of any type of variation (slow, abrupt) as long as it has an impact on the trend of the time-series. This method has been found to be less affected by the seasonal variability of vegetation and thus more performant to detect abrupt changes in the vegetation structure due to forest cut (Ruiz-Ramos et al., 2020).

To monitor forest cover changes, many studies have used pairwise or single epoque image comparison or multi-temporal averages for detecting changes between two dates (Antropov et al., 2016; Bouvet et al., 2018; Joshi et al., 2015; Lievens et al., 2017; Reiche et al., 2018b;

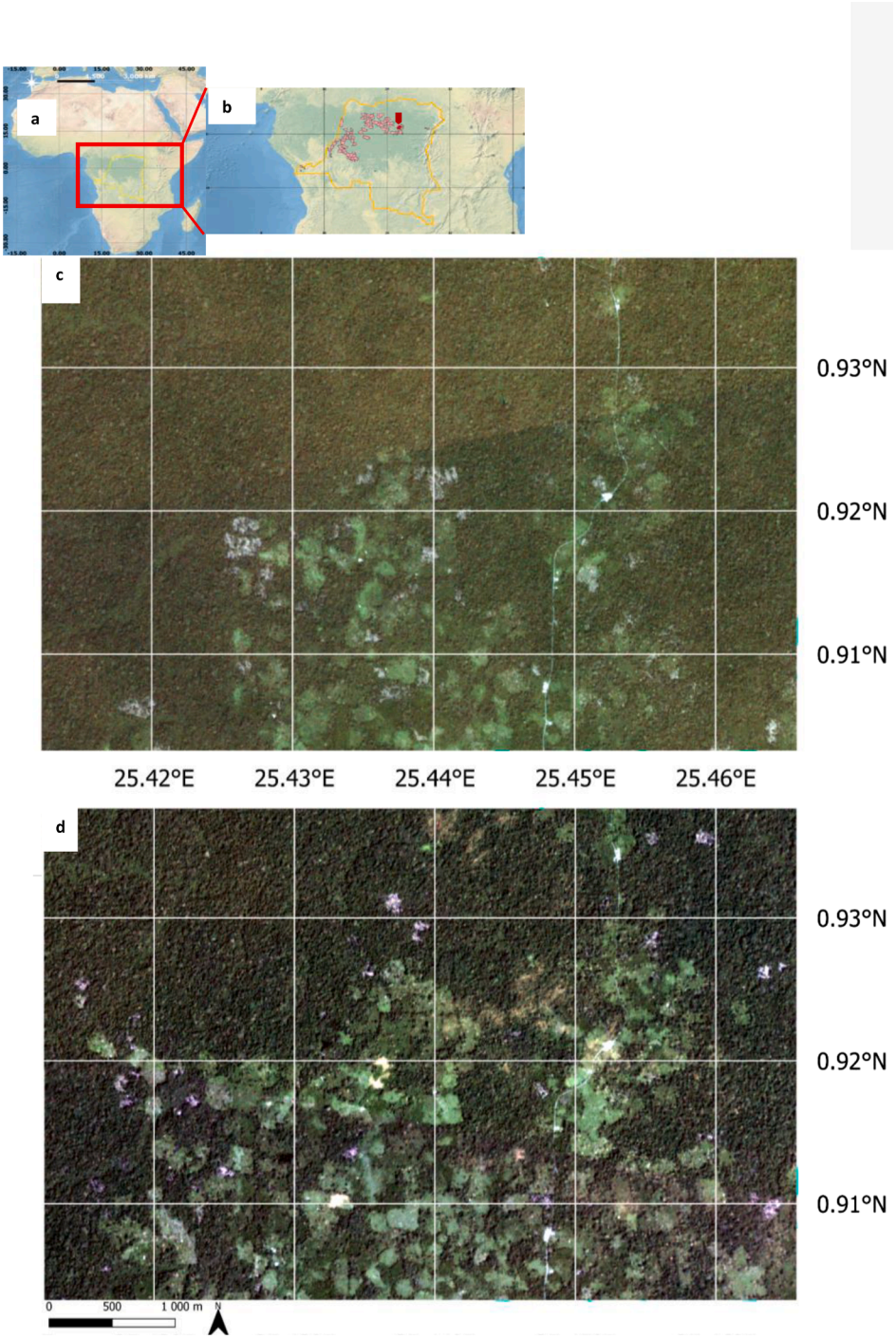

Fig. 1. Study site: (a) global view including DRC borders, (b) global view including DRC borders with its forest concessions. The study zone is indicated by the red pinpoint. PlanetScope 3 m surface reflectance image over the study site dated from (c) 2018–01-06 and (d) 2019–11-29. (For interpretation of the references to color in this figure legend, the reader is referred to the web version of this article.)

Rüetschi et al., 2019; Tanase et al., 2015; 2010). These methods have known limits: there is often a delay between a change in the vegetation structure and/or cover and a change in the SAR backscattering. Due to the SAR sensitivity to changes in the vegetation/soil moisture content and surface roughness, vegetation change is difficult to detect or may be detected with a delay (Belenguer-Plomer et al., 2019; Reiche et al., 2018a; Ruiz-Ramos et al., 2018; Watanabe et al., 2018). Moreover, if the revisit time of the satellite is too low, vegetation may partially recover after being cut, hindering the detection of the cut (Numbisi and Van Coillie, 2020; Reiche et al., 2021). Though L-band SAR images can be used for an accurate monitoring of the deforestation in tropical environments e.g., (Takeuchi et al., 2001; Whittle et al., 2012), they are not easily available and often have a lower temporal resolution. The use of time-series with a high temporal resolution such as Sentinel-1 allows early detection and permits to detect changes at different time scales and to reduce the noise in the backscatter signal due to speckle or temporary changes.

In this study, C-band SAR observations from Sentinel-1 A satellite were used to monitor deforestation and other forest cover changes in the living area of a legal forest concession of the Democratic Republic of Congo (DRC). This satellite, launched in 2014, has a 12-day revisit period over the DRC and a spatial resolution of 20 m × 22 m, allowing to monitor changes in vegetation with a high resolution in both space and time. We evaluated the use of the CuSum algorithm (Manogaran and Lopez, 2018) applied to dual polarization VV-VH observations, taking advantage of the high capability of CuSum to detect vegetation cover change (Ruiz-Ramos et al., 2020). Results based on the combination of different configurations of the CuSum approach are analysed and optimal configurations are presented and discussed.

2. Study site and data

2.1. Study site

For the investigation of forest change in the Congo Basin by developing using our approach, we chose to monitor the forest near the living area of a forest concession where degradation and deforestation are likely to occur. The concession is the Industrie Forestière du Congo (IFCO) COD 018/11 forest concession (Alibuku), located within the North-Eastern region of Kisangani in the Democratic Republic of Congo (DRC), in central equatorial Africa (Fig. 1). The climate of the region is characterised by two wet seasons, reaching their peaks in terms of rainfall respectively at the end of March / early April and end of September / early October and two dry seasons per year. The maps of the forest concessions are available at the DRC forest atlas (Forest Atlas, 2016) available at https://cod.forest-atlas.org/. This concession is formed of yearly allowed cut zones where trees are extracted and in a living area for the logger community. The study site was specifically selected based on the nature/typology of the expected forest change. Since most of the forest changes were expected to be made by logger communities (over-exploitation for timber and firewood, agricultural activities (Contreras-Hermosilla et al., 2000)) instead of commercial logging clear-cuts, the study site was located near the populated area of the Alibuku concession. The study site (area = 22.57 km^2) is located between 25.4122° and 25.4657° E, and 0.9033° and 0.9376° N, in the north-western part of a living area.

2.2. Data

2.2.1. Sentinel-1 SAR images

The Sentinel-1 mission, developed by the European Space Agency (ESA) in the framework of the Copernicus programme, is a constellation composed of 2 satellites positioned on the same reference orbit plane with a 180° orbital phasing difference at an altitude of 693 km (Torres et al., 2012). The sun-synchronous orbit is near polar, presenting an inclination of 98.18°. The repeat cycle of each satellite is 12 days over the study site. Sentinel-1A was launched on April 3rd of 2014, while Sentinel-1B was launched on April 25th 2016. The main instrument onboard both Sentinel-1 satellites is a C-band Synthetic Aperture Radar (SAR) referenced as C-SAR. It is operating at a frequency of 5.405 GHz in 4 different modes, of which the Interferometric Wide-swath (IW) with a ground resolution of 20 m × 22 m, at the VV and VH polarizations was selected in this study. The images are available in several formats: Slant Range, Single Look Complex (SLC), Ground Range, and Multi-Look Detected (GRD). The data used in this study are the GRD products in IW mode at the VV and VH polarizations. The images used in this study were only acquired from Sentinel-1 A on a single descending orbit at the sampling period of 12 days as no Sentinel-1B images were available on the study area. The resulting pixel size is 10 m × 10 m. This product was chosen instead of the SLC as it is a good compromise in terms of possible speckle noise reduction and volume of data to get accurate data but not increasing too much the computational time. A total of 60 images that formed our time-series on the study site between 01/01/2018 and 01/01/2020 were provided by the European Space Agency (ESA) at and downloaded using VtWeb (https://visioterra.org/VtWeb/).

2.2.2. PlanetScope optical images

To evaluate our Sentinel 1 detection algorithm, a reference map of the forest changes was created using high-resolution PlanetScope images. We used the level 3B product of PlanetScope Ortho Scene obtained from a multispectral Cubesat constellation. This product is a 4-band (Red: 605–695 nm, Green: 515–595 nm, Blue: 450–515 nm, NIR: 740 – 900 nm) Surface Reflectance (SR) image, orthorectified and scaled, with a pixel resolution of 3 m. The PlanetScope images available during the period ranging from 06/01/2018 to 30/12/2019 were selected upon the following criteria: (i) Images on which the visual interpretation was not possible because of large cloud cover were removed. No strict threshold on cloud cover could be used as the visualization depends on the thickness of the clouds. For instance, it was possible to perform visual interpretation if the cloud cover corresponds to a thin cloud veil covering the whole scene. (ii) Images partially covering the scene and images separated by a day or less from one another were removed. After this selection step, only twenty-four images were kept. Among the kept images, some of them were still affected by the presence of a few clouds that did not prevent to perform a visual interpretation. The images were downloaded from Planet Explorer at https://www.planet.com (Planet, 1996).

2.2.3. Tree cover loss map from global forest watch

To compare with the results obtained from the CuSum change detection algorithm applied to Sentinel-1 SAR images, the performances of the Global Forest Watch (GFW) Tree Cover Loss (TCL) map (Hansen et al., 2013) were also evaluated against the visual interpretation of the PlanetScope images. Results obtained from this forest change cover analysis were subsequently used for assessing the performance of our detector. The TCL map is a dataset developed for monitoring forest cover loss worldwide based on Landsat-5 TM, Landsat 7 ETM+, Landsat 8 OLI/TIRS and MODIS data with a pixel resolution of 30 m (Potapov et al., 2020). The TCL map over the study site is made freely available at https://data.globalforestwatch.org/ (Dataset: 'Granule 10N 20E' on GFW website). According to the TCL map, the study zone lost about 204 ha of tree cover (Fig. 2) between 2018 and early 2020.

3. Methods

3.1. Pre-processing

The Sentinel-1 SAR images were pre-processed using VtWeb. VtWeb is an online platform enabling users to easily browse free Earth observation data, display it in 2D/3D and process it on-the-fly (VtWeb, 2015) accessible on https://visioterra.org/VtWeb/. The pre-processing performed by VtWeb to obtain geo-corrected backscatter images (resulting

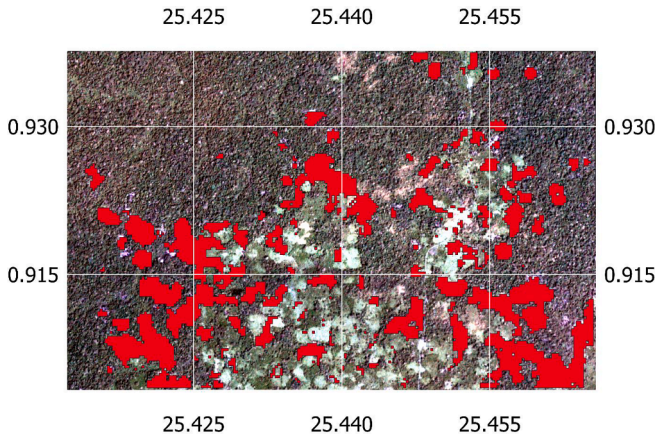

Fig. 2. TCL map (Hansen 2018–2019) on the PlanetScope 2019–11-29 image background.

in γ^0 terrain corrected data) consisted in the 3 following steps (Fig. 3):

- Orbit correction
- thermal noise removal (Piantanida and Miranda, 2017),
- terrain flattening as terrain correction to remove topological and incidence effects (Small, 2011).

The speckle was filtered using the bilateral filter made available in the python PyRAT Toolbox (Reigber et al., 2019) with a kernel window size of 7 × 7. This filter is a spatial filter presenting the advantage of preserving edges in the images. Its filtering principle relies on the replacement of a pixel value with the weighted pixel value average in the kernel (Tomasi and Manduchi, 1998).

3.1.1. Haralick textures and image selection

VtWeb provides different levels of aggregation of the Sentinel-1 SAR images ranging from the highest pixel resolution (10 m) to a very low pixel resolution (40960 m). The Contrast (CON) from Haralick textures (Coelho, 2013; Haralick et al., 1973) was computed on aggregated images with a resulting pixel resolution of 1,280 m to monitor changes in the SAR backscatter at a larger scale than that of S1 (10 m × 10 m) as follows:

$$CON = \sum_i \sum_j p(i,j)*(i-j)^2 \quad (1)$$

where *p(i,j)* is the frequency of the elements in Grey Level Co-Occurrence Matrix (GLCM),(i,j) is the cell index.

The study zone is located in a region characterized by a high cloud cover during the entire year. The presence of raincells has been confirmed on this area. Raincells are known to cause either an enhancement and/or a darkening of the SAR images (see an example of this latter effect on Fig. 4). These two opposite effects are due to the presence of hydrometeors which interact with the EM waves emitted by the SAR sensor, causing dark and bright areas, on the SAR images, especially at C and X-bands (Alpers and Melsheimer, 2004; Kellndorfer, 2019; Users Manuals, 2021). To detect the presence of large raincells in the SAR images, the Haralick texture features were used. The presence of raincell strongly modifies the CON parameter as defined in Eq. (1).

The removal of raincell-contaminated images was automatized using a threshold (τ) defined using the temporal dynamics of CON in both the VV and VH polarizations:

$$\tau = K*(\sigma_{CON} + \overline{CON}) \quad (2)$$

where $\overline{CON}$ and σ_{CON} are respectively the average and the standard deviation (std) of CON during the observation period, and K a constant empirically set equal at 2 in this study. If *CON* is greater than τ in a Sentinel-1 image for both the VV and VH polarizations, the S1 image is removed from the analysis. A large raincell was observed on the image acquired on 13/11/2018. This image was removed from the analysis (Fig. 5).

3.2. Change detection algorithm

3.2.1. CuSum algorithm

The Cumulative Sum (CuSum) algorithm is a change point detection method based on time-series analysis. It has been initially used in the financial sector (Manogaran and Lopez, 2018) and pioneer studies have applied it for mangrove and temperate forest monitoring (Kellndorfer, 2019; Ruiz-Ramos et al., 2020). Previous studies showed better performances in deforestation detection when this method was applied to filtered and smoothed time-series (Kellndorfer, 2019). The C-band SAR backscatter signal tends to decrease after a forest cut, according to literature (Kellndorfer, 2019). The CuSum method is able to detect such changes in the signal (Manogaran and Lopez, 2018). The CuSum method consists in 5 steps including the bootstrap analysis.

The first step is to compute the VV and VH backscatter time-series of each pixel of the Sentinel-1 image in the study area over a given period. Then, the mean of the time-series ($\overline{\gamma^0}$ (j), over each pixel j) is determined at both the VV and VH polarizations and used in the computation of the cumulative sum of the residuals, R_{sumj}:

$$R_{sumj} = \sum_{i=1}^{n_{images}} R_{ij} \quad (3)$$

where $R_{ij} = \gamma^0_{ij} - \overline{\gamma^0_j}$, n_{images} is the number of images and j the pixel index.

The third step consists in determining the maximum and minimum value of the cumulative sum of the residuals to compute the amplitude A_{sumj} over the period:

$$A_{sumj} = R_{sum\_maxj} - R_{sum\_minj} \quad (4)$$

where R_{sum_maxj} is the maximum value of R_{sumj} and R_{sum_minj} is the minimum value of R_{sumj}. The date of change in the vegetation over the pixel j is assumed to happen at the date when R_{sumj} reaches a maximum. A bootstrap analysis based on A_{sumj} is then conducted to validate or invalidate the change. There is no global threshold over the magnitude of the change. A threshold is computed individually over each pixel, as the mean value of the time series may change from one pixel to another.

3.2.2. Bootstrap analysis

A bootstrap analysis is conducted on the CuSum result. The bootstrap analysis is a mean to check the validity of the change detected through an indirect measure of the impact of the order sequence on the times-series. The bootstrap consists in conducting CuSum on a randomly modified backscatter timeseries $n_{bootstraps}$ times and check if the generated amplitude of the residuals is greater than the original amplitude of the residuals. $n_{bootstraps}$ is the number of bootstraps. It depends on the length of the time-series (Kellndorfer, 2019). Firstly, the original backscatter time-series is randomly reorganized, thus modifying the temporal order. Then, the CuSum method is applied to the newly reorganized series to compute $R_{sum\_randj\_i}$ and $A_{sum\_randj\_i}$ (with i the index of the bootstrap). The next step is to compute the difference of amplitude between A_{sumj} and $A_{sum\_randj\_i}$ (Eq.6)

$$n_{bootstraps} = \begin{cases} n_{images}!(if\, n_{images}! < 1500) \\ 1500(if\, n_{images} \geq 1500) \end{cases} \quad (5)$$

where $n_{images}!$ is the factorial of the number of images.

$$A_{diffj_i} = A_{sumj} - A_{sum\_randj_i} \quad (6)$$

If $A_{diffj\_i} > 0$, the residual amplitude of the randomly generated reorganized time-series ($A_{sum\_rand\_i}$) is lower than its original value (before reorganization). This means the original residual amplitude

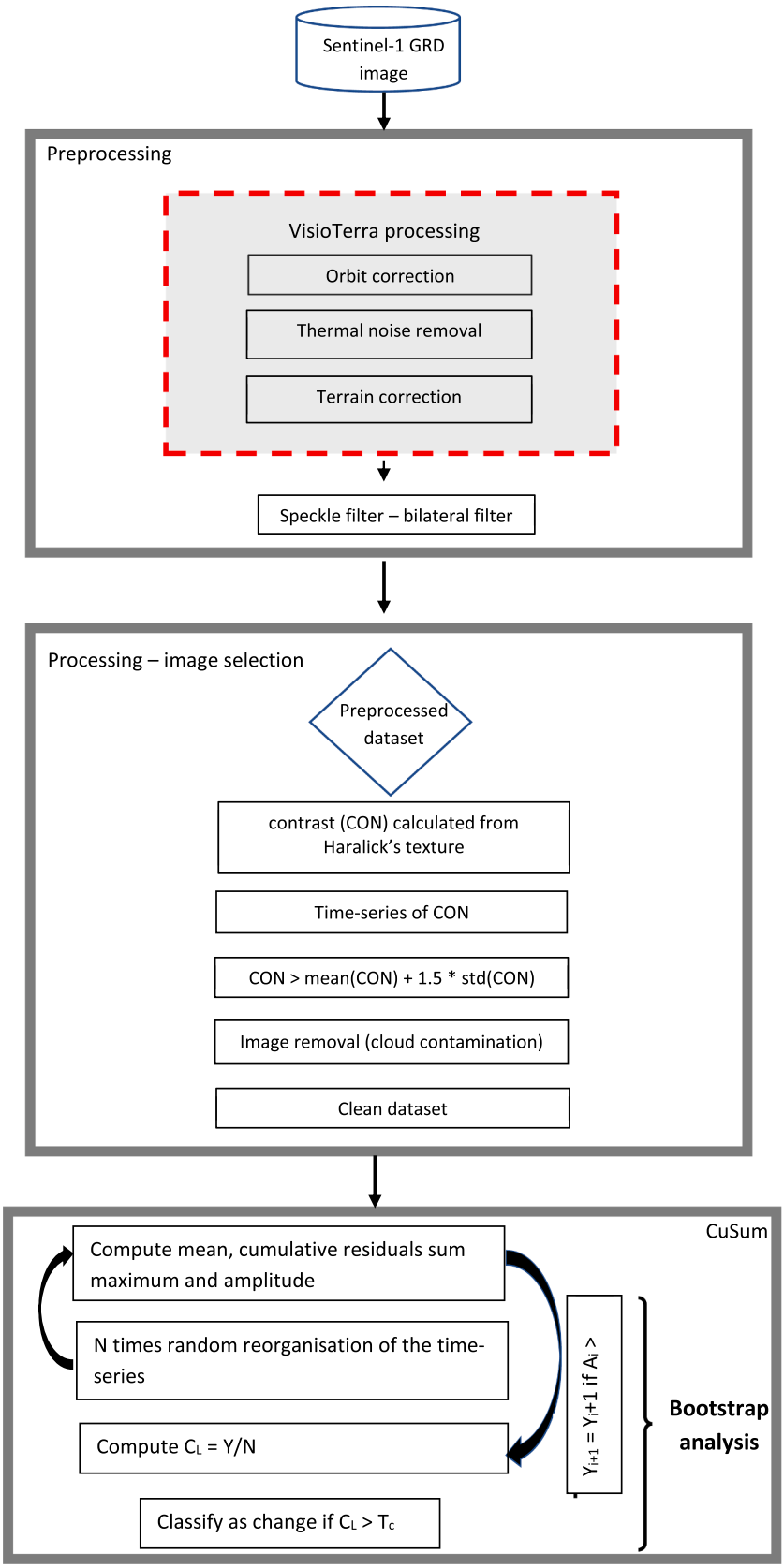

Fig. 3. Workflow of the Sentinel-1C-SAR image preprocessing, processing and CuSum steps.

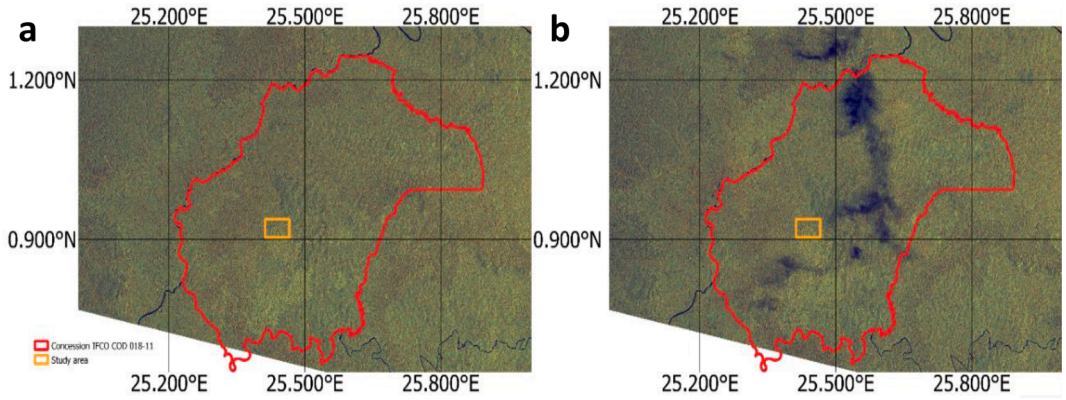

Fig. 4. Sentinel-1 SAR images dated from (a) 20/10/2018 and (b) 13/11/2018 displayed in RGB: VV, VH, NDI(VV,VH). The raincell effect is visible on the second image.

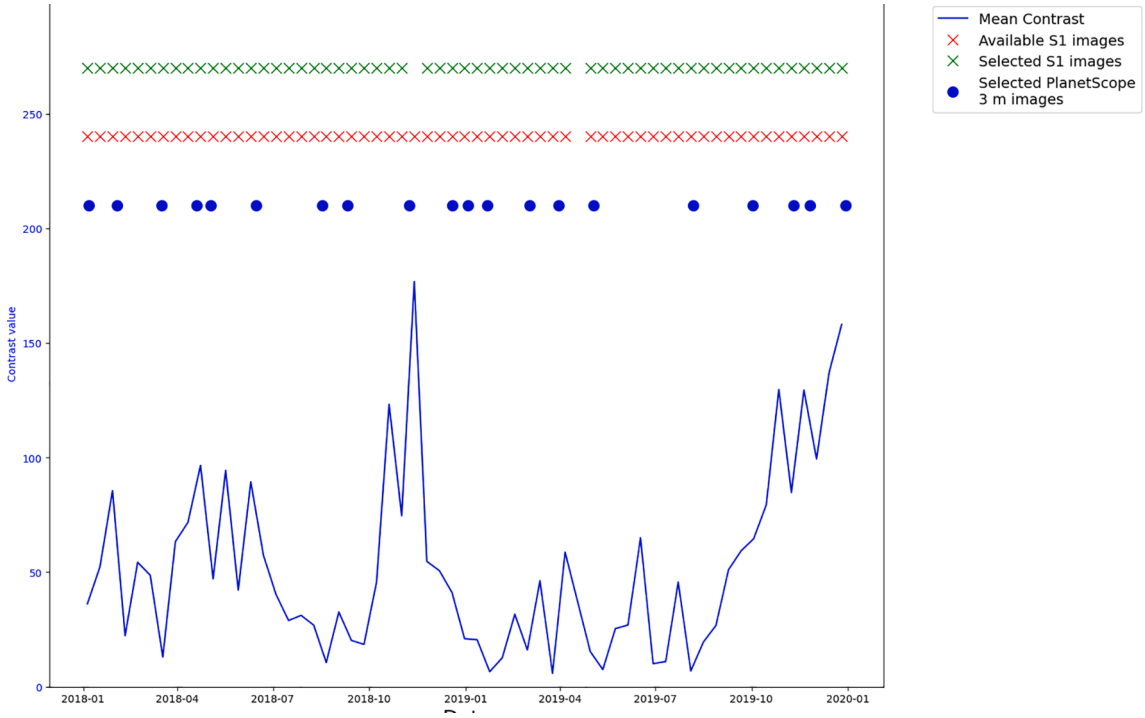

Fig. 5. Temporal availability of Sentinel-1C-SAR IW dual polarization and PlanetScope 3 m images. The 13/11/2018 Sentinel-1 image was removed due to partial raincell contamination. The Contrast is computed from Haralick's texture (see 3.2), showed on VV polarisation. The Mean Contrast is the average contrast of a Sentinel-1 image with a pixel resolution of 1280 m over the study area.

(A_{sumj}) is affected by the temporal dimension. The number of times the original residual time-series presents a A_{sumj} value greater than the randomly reorganised one is estimated and referred to as the index N_{gj} (Eq. 7). This index is incremented by 1 each time $A_{diffj\_i} > 0$. It is an indirect measure of the sequence effect in the backscatter time-series and a sensitivity parameter that intervenes in the computation of the Confidence Level (CL_j, Eq. 8).

$$N_{Gj} = \sum_{i=1}^{n_{bootstraps}} Index_{Gji} \tag{7}$$

$$\text{With } Index_{Gji} = \begin{cases} 1 if A_{diffj_i} > 0 \\ 0 if A_{diffj_i} \leq 0 \end{cases}$$

$$CL_j = \left(\frac{N_{Gj}}{n_{bootstraps}}\right) \tag{8}$$

CL represents the ratio of bootstraps in which the original backscatter time-series presents the amplitude $A_{sumj} > A_{randj}$ in comparison to the total number of bootstraps. A critical threshold value (T_c) can be set as a CL over which the change point is considered as valid by the bootstrap analysis.

3.2.3. Sensitivity to input parameter

The Confidence Level (CL) is a criterion related to the algorithm's sensitivity. In this study, we evaluated four different critical thresholds T_c based on the Confidence Level over which we consider the change as valid: $T_c = 0.25$, 0.50, 0.75 and 1.00. Higher T_c values resulted generally in a lesser number of pixels detected as "change" since only "change" pixel with high confidence level will reach the specific threshold, whereas lower T_c values resulted generally in a higher number of pixels detected as "change" because the lower specific threshold will be crossed on many pixels.

3.2.4. Spatial operations over the CuSum results

The two maps resulting from application of the CuSum algorithm to the VV and VH SAR images were intersected to form the "VV intersect VH" dataset. In that case, a pixel is considered to be subject to a change when it is classified as 'change' at both the VV and VH polarizations. This dataset was made in order to assess if changes affect both volume and surface components. As the SAR backscatter is affected by the dominant scattering mechanism resulting from the signal/target interaction, the impact on polarisation channels can vary. A dominant surface or double-bounce scattering mechanism generally display a higher intensity on the VV channel, while a dominant volume scattering will greatly influence the VH backscatter signals. The changes affecting an area can modify these interactions, resulting in changes being more detected by a polarisation than by the other.

The maps based on the VV and VH results were joined to form the "VV union VH" dataset. In that case, a pixel is considered to be subject to a change when it is classified as "change" from at least one of the polarizations (either VV or VH). Our objective with these "intersection" and "union" maps were to check the consistency / difference of the results based on both the VV and VH polarizations and to evaluate their complementarity.

High threshold values of T_c ($T_c = 1.00$) were found to be the most robust values in terms of accuracy from preliminary tests. In order to reduce the number of false positives obtained from low T_c values in the form of small clusters of change, a spatial recombination of T_c thresholds was applied. Results obtained from high T_c values were combined with those obtained from low T_c values. The raster images were first converted to vector images containing changes as polygons by using a 4-pixel connexion. Secondly, the areas corresponding to "high T_c" polygons (polygons to computed from high T_C values) were selected and only polygons of area $> 300\ m^2$ were kept. They composed the base on which the following filter was applied. A filter was then applied using lower T_c values. Only the "low T_c" polygons including a "high T_c" polygon were kept in the analysis (Annexe 2). This resulted in the cross-T_c results, also referred to as 100_25 (base: $T_c = 1.00$, low $T_c = 0.25$), 100_50 (base: $T_c = 1.00$, low $T_c = 0.5$) and 100_75 (base: $T_c = 1.00$, low $T_c = 0.75$).

3.3. Validation steps

3.3.1. 3.3.1. Reference map composition

The resulting maps of the date of forest change occurrence obtained in this study were evaluated using the PlanetScope optical images as no in-situ information was available. The GFW maps were not used as the visual inspection showed they missed newly deforested areas compared to the ones observed on the PlanetScope images, and hence, were considered to be less reliable over the study zone. Eventually, all the areas visually determined as newly deforested from the consecutive PlanetScope images over the 2018–2019 period were assembled to form the PlanetScope 2018–2019 cover change image. This image was used as a reference to assess the accuracy of the change detection method based on the CuSum algorithm applied to the Sentinel 1 images. The 'deforestation' considered in the following parts of this study was the visual interpretation of change from forest to non-forest. The 'degradation' considered in the following parts of this study was estimated from the visual interpretation of PlanetScope images. It corresponds to the changes in the radiance of forested areas before their deforestation.

3.3.2. Statistics

There are two types of errors when comparing two binary spatial datasets: i) the false positive, which corresponds to the reference map detecting no change while the algorithm detects a change, ii) the false negative, which occurs when the reference map detects a change whereas the algorithm does not detect it. In order to describe the quality of the matching between our S1-based retrieved change map and the reference PlanetScope change map, the following classical statistical indicators (Overall Accuracy as Accuracy, Recall, Precision, F-score and Kappa Coefficient) derived from the confusion matrix were used. Due to class imbalance between Change and No Change, the overall accuracy, recall and precision should be studied along with F-score and Kappa coefficient for interpretation. The overall accuracy is shown here as an indicative statistic and should not be interpreted by itself, as explained in Olofsson et al. (2014) which provides exhaustive information about good practices for land cover change estimates. The overall accuracy is the ratio between the number of correctly classified pixels and the total number of pixels.

$$Accuracy = \frac{TP + TN}{TP + TN + FP + FN} \tag{9}$$

where TP are the True Positive (pixels classified by both the reference map and the algorithm as 'cover change'), TN are the True Negative (pixels classified by both the reference map and the algorithm as 'no cover change'), FP are the False Positive errors and FN are the False Negative errors. The precision corresponds to the ratio between the number of pixels correctly classified as 'cover change' and the total number of pixels classified as 'cover change' by the algorithm.

$$Precision = \frac{TP}{TP + FP} \tag{10}$$

The recall corresponds to the ratio between the number of pixels correctly classified as 'cover change' and the total number of pixels classified as 'cover change' by the reference map.

$$Recall = \frac{TP}{TP + FN} \tag{11}$$

The F1-score is the weighted average of precision and recall. This score is used when the classes are unevenly distributed.

$$F1 = 2\frac{recall.precision}{recall + precision} \tag{11}$$

The Kappa Coefficient is a measure quantifying how better the algorithm performs compared to a random classification according to the frequency of each class.

$$\kappa = \frac{P_0 - P_e}{1 - P_e} \tag{12}$$

where P_o is the Observed Accuracy (Eq.9) and P_e the expected accuracy.

$$P_e = \frac{TP + FP}{Total}.\frac{TP + FN}{Total} + \frac{TN + FN}{Total}.\frac{TN + FP}{Total} \tag{13}$$

4. Results

Results obtained from the investigation of the PlanetScope data revealed a cover change area estimated at 341.5 ha (15.1% of the total study area) over the 06/01/2018 – 26/11/2019 period.

4.1. Spatiotemporal distribution of the changes

The CuSum algorithm was applied on the time-series of backscattering coefficients from the Sentinel-1 SAR images acquired at C-band in both the VH and the VV polarisations, for T_c values of 0.25, 0.5, 0.75 and 1.00. Cover changes detected by the CuSum approach are presented in Fig. 6a to d, and 7-a to d, respectively for VH and VV. Change pixels are developed in continuous and consistent spatial patterns. For all mapping configurations (in terms of polarisation and T_c values), the number of pixels affected by a change decreases as T_c increases: the total area presenting a change ranges from a minimum value of 113.2 ha (VV intersect VH, $T_c = 1$) to a maximum value of 1333.6 ha (VV union VH, $T_c = 0.25$). Smaller clusters affected by changes are generally detected for lower values of T_c than for higher values. Besides, the cluster size is also greater for lower values of T_c than for higher T_c values. The use of higher T_c values lowers the number of these clusters, but also reduces

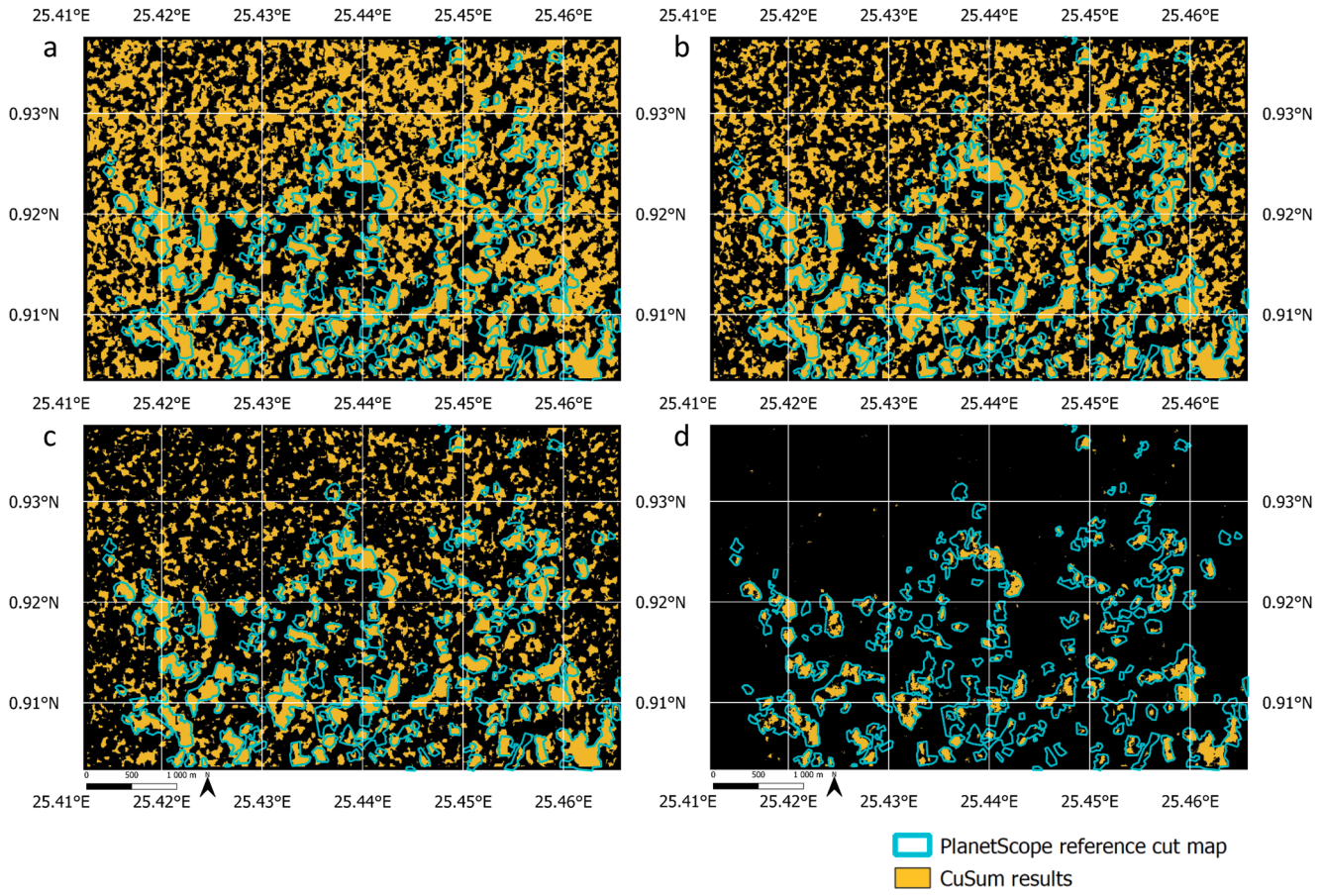

Fig. 6. CuSum algorithm results at VH polarization with T_c = (a) 0.25, (b) 0.50, (c) 0.75, (d) 1.00 with PlanetScope reference map cuts as blue-colored polygons. (For interpretation of the references to color in this figure legend, the reader is referred to the web version of this article.)

the size of the larger clusters. The latter are most often connected whereas the small clusters are not.

The results of the change detection method were compared with the PlanetScope reference map. Results obtained for a lower T_c value of 0.25 show a better detection of the cut areas with lower false negatives (True Positives = 273.7 ha / False Negatives = 67.8 ha for VV union VH) than for higher T_c values of 1 (True Positives = 160.5 ha / False Negatives = 181.1 ha for VV union VH). However, results obtained for lower T_c values (T_c = 0.25) present a large number of false positives (1060.0 ha for VV union VH) compared to higher T_c values of 1 (327.7 ha for VV union VH, Table 1). It is worth noticing that the larger clusters of change detected for any VV and VH combinations and for any T_c values correspond to the areas detected as cut in the PlanetScope reference map.

When comparing the results of the CuSum algorithm applied to the polarization channels, the VV channel detects more small clusters of change compared to the results obtained at VH. Similar results were obtained when comparing VV with VV union VH results. The area of the largest clusters was lower for VV (True Positives = 230.9 ha and False Negatives = 110.6 ha for T_c = 0.25, True Positives = 136.6 ha and False Negatives = 205.0 ha for T_c = 1.00). The clusters based on the VV polarization are more isolated than those obtained at VH polarization. For low Tc values (high sensitivity to changes), less changes are detected using VV than using VH, but it is the opposite for a higher T_c value.

According to Table 2, the number of separated clusters of change is not proportional to the threshold. This could be explained as the bigger clusters can often be dissociated at higher T_c, but smaller T_c clusters can disappear at higher T_c. The cross-threshold operations result in increasing mean and median areas compared to their simple T_c equivalent.

4.2. Cross comparison against external datasets using confusion-matrix derived statistics

When comparing results obtained for all mapping configurations based on VV, VH and their combinations (intersection and union) and for any T_c value (0.25, 0.5, 0.75, 1 and 100_25, 100_50 and 100_75), the precision ranges from very low (0.21 for VV union VH for T_c = 0.25) to high (0.93 for VV intersect VH for T_c = 1.00). Precision is very similar for all mapping configurations for T_c = 1.00 (0.87 to 0.90). The results of the different mapping configurations are very scattered for T_c ranging from 0.25 to 0.75. The cross-Tc combination generally increases the precision (compared to the simple T_c configuration), for instance the precision increased by 11.0% for VH (compared to T_c = 0.5 against 100_50) or by 23.8% for VV intersect VH (compared to T_c = 0.25 against 100_25) (Fig. 7). However, the use of cross-Tc does not significantly increase the precision for VV union VH (for T_c = {0.25; 0.50} against {100_25; 100_50}) and for VH (T_c = 0.25 against 100_25). Whatever the T_c values, the VV intersect VH presents a better precision, followed by simple VV with a difference in precision of 0.11 (Table 3).

The accuracy results range from acceptable (50% for VV union VH at T_c = 0.25) to very accurate (91% for VV intersect VH at 100_75). The range of results is larger for lower T_c values than for higher ones. The use of cross-T_c leads to a narrower range of the accuracy values, increasing the accuracy from 2% to 10%. The most stable accuracy values were observed for VV intersect VH, with accuracy ranging from 81% to 91%. For VV intersect VH, the accuracy results obtained for T_c = 1.00 are similar to those obtained for cross-Tc = 0.75.

Lower recall values were obtained for higher T_c values (Fig. 8). The range of the Recall values is 0.34–0.78 considering all combinations of

Table 1
Comparison between the CuSum results and the reference map. Change area of reference (from PlanetScope images) = 341.5 ha, non-change area of reference = 6581.1 ha. c = change area, nc = non-change area, TP: True Positives, TN: True Negative, FP: False Positive, FN: False Negative. The color legend is qualitative: red is considered as "poor", orange as "relatively poor", yellow as "relatively good" and green as "good".

Base	T_c	TP (ha)	TN (ha)	FP (ha)	FN (ha)
VV	0.25	230.9	1426.1	488.9	110.6
	0.50	227.5	1501.6	413.5	114.0
	0.75	217.8	1641.2	273.9	123.8
	1.00	136.6	1895.4	19.7	205.0
	100_25	219.9	1719.6	195.5	121.7
	100_50	217.1	1764.6	150.5	124.5
	100_75	208.6	1810.5	104.6	133.0
VH	0.25	261.3	1029.8	885.2	80.3
	0.50	253.8	1193.9	721.2	87.8
	0.75	239.7	1453.0	462.1	101.9
	1.00	128.2	1893.8	21.3	213.4
	100_25	259.5	1153.3	761.8	82.0
	100_50	249.1	1491.1	424.0	92.4
	100_75	231.6	1718.7	196.4	109.9
VV union VH	0.25	273.7	855.1	1060.0	67.9
	0.50	269.7	1007.8	907.3	71.9
	0.75	258.4	1296.1	618.9	83.1
	1.00	160.5	1882.3	32.8	181.1
	100_25	273.0	895.9	1019.2	68.5
	100_50	267.7	1257.5	657.6	73.8
	100_75	252.8	1614.6	300.5	88.7
VV intersect VH	0.25	218.9	1599.4	315.6	122.7
	0.50	212.2	1686.5	228.5	129.4
	0.75	199.2	1797.5	117.6	142.3
	1.00	104.9	1906.9	8.2	236.6
	100_25	200.4	1806.2	108.9	141.2
	100_50	196.4	1829.7	85.3	145.2
	100_75	187.4	1858.4	56.7	154.1
		Legend	Legend	Legend	Legend
		<85 (<25% c)	<479 (<25% nc)	>256 (>75% c)	>256 (>75% c)
		85-171 (25-50%)	479-958 (25-50%)	256-171 (75-50%)	256-171 (75-50%)
		171-256 (50-75%)	958-1436 (50-75%)	171-85 (50-25%)	171-85 (50-25%)
		>256 (>75%)	>1436 (>75%)	<85 (<25%)	<85 (<25%)

polarisations. This range is larger for $T_c = 0.75$ than for $T_c = 0.25$, 0.50 or 1.00 considering all possible combinations of VV and/or VH. The best recall values at all T_c and cross-T_c were obtained with VV union VH, increasing up to 0.78 for cross-T_c = 100_25.

The Kappa coefficient values range from very low (0.12) to acceptable (0.59) considering all VV and/or VH combinations. The range of the Kappa coefficient values is larger for lower T_c values. Use of cross-Tc configurations increases the Kappa coefficient by 13.5%. Overall, the higher value of the kappa coefficient is obtained using VV intersect VH.

The F1-score results range from relatively low (0.33) to acceptable (0.64) considering all VV and/or VH combinations. Use of cross-Tc configurations increases the F1-score by 4% up to 15%. Overall, the higher value of the F1-score is obtained using VV intersect VH.

5. Discussion

Raincells are a large source of contamination of the backscatter coefficient over tropical forests. When applying the CuSum algorithm, we noted that it is crucial to filter out the images affected by the presence of raincells. If not, the inclusion of a contaminated pixel in the temporal

Table 2
Spatial comparison between the CuSum clusters of change detected.

Base	T_c	Number	mean area (ha)	median (ha)
VV	0.25	1711	0.4207	0.0544
	0.50	2054	0.3121	0.0453
	0.75	1972	0.2493	0.0453
	1.00	453	0.3449	0.0272
	100_25	122	3.4043	1.65
	100_50	122	3.013	1.4505
	100_75	138	2.2695	1.1785
VH	0.25	583	1.9666	0.0453
	0.50	1077	0.9053	0.0635
	0.75	1522	0.4611	0.0725
	1.00	525	0.2847	0.0181
	100_25	41	24.9114	3.6535
	100_50	77	8.7425	2.7016
	100_75	115	3.7219	2.1486
VV union VH	0.25	574	2.3235	0.0181
	0.50	1041	1.1307	0.0272
	0.75	1953	0.4492	0.0453
	1.00	586	0.3297	0.0181
	100_25	29	44.561	0.5802
	100_50	55	16.8254	2.9645
	100_75	117	4.7293	2.1576
VV intersect VH	0.25	1609	0.3322	0.0544
	0.50	1703	0.2587	0.0363
	0.75	1160	0.2731	0.0363
	1.00	240	0.4715	0.0725
	100_25	92	3.3616	2.0229
	100_50	97	2.9045	1.7973
	100_75	101	2.417	1.514

average of the backscatter is likely to impact the results of the change detection method. In the present study, we found that the Contrast parameter from the Haralick's textures provided an efficient way to detect the contaminated images.

The lack of in-situ data complicates the validation process of the surfaces identified as presenting a cover change. By using visual interpretation of PlanetScope high resolution (3 m) images, clear cuts, field cuts and field cover changes could be clearly identified. The visual interpretation permitted to clearly separate forest and non-forest areas, and the changes occurring over these two types of covers. The validation of the method presented above was limited to clear cuts from forest areas, but changes over non-forest areas could be also detected using our approach, showing that this technique is able to detect forest cuts and forest degradation but also crop field cuts and soil cover changes.

High precision (0.93), recall (0.80), accuracy (91%), were obtained by evaluating the results of different parameterizations of the CuSum algorithm against PlanetScope, used as a reference, but the value of the Kappa coefficient remains relatively average (0.59 for the best configuration). The statistics of the comparison between the GFW map and the PlanetScope reference map show that, over the study area, the GFW map presents high accuracy (86%), but average precision (0.54), recall (0.57) and Kappa coefficient (0.48). The Tree Cover Loss area estimated from GFW dataset was 204 ha (9.0 % of the study area) *vs* 341.5 ha (15.1 % of the study area) for the PlanetScope-based reference map. The results of our method applied to Sentinel-1 SAR images has a higher Kappa coefficient than GFW in spite of being impacted by large false positives. Several clusters detected using the CuSum approach to the Sentinel-1 SAR images did not correspond to cuts based on the PlanetScope visual interpretation. As it can be seen in Fig. 9, several zones were detected "as cover changes" by applying CuSum before the zones were

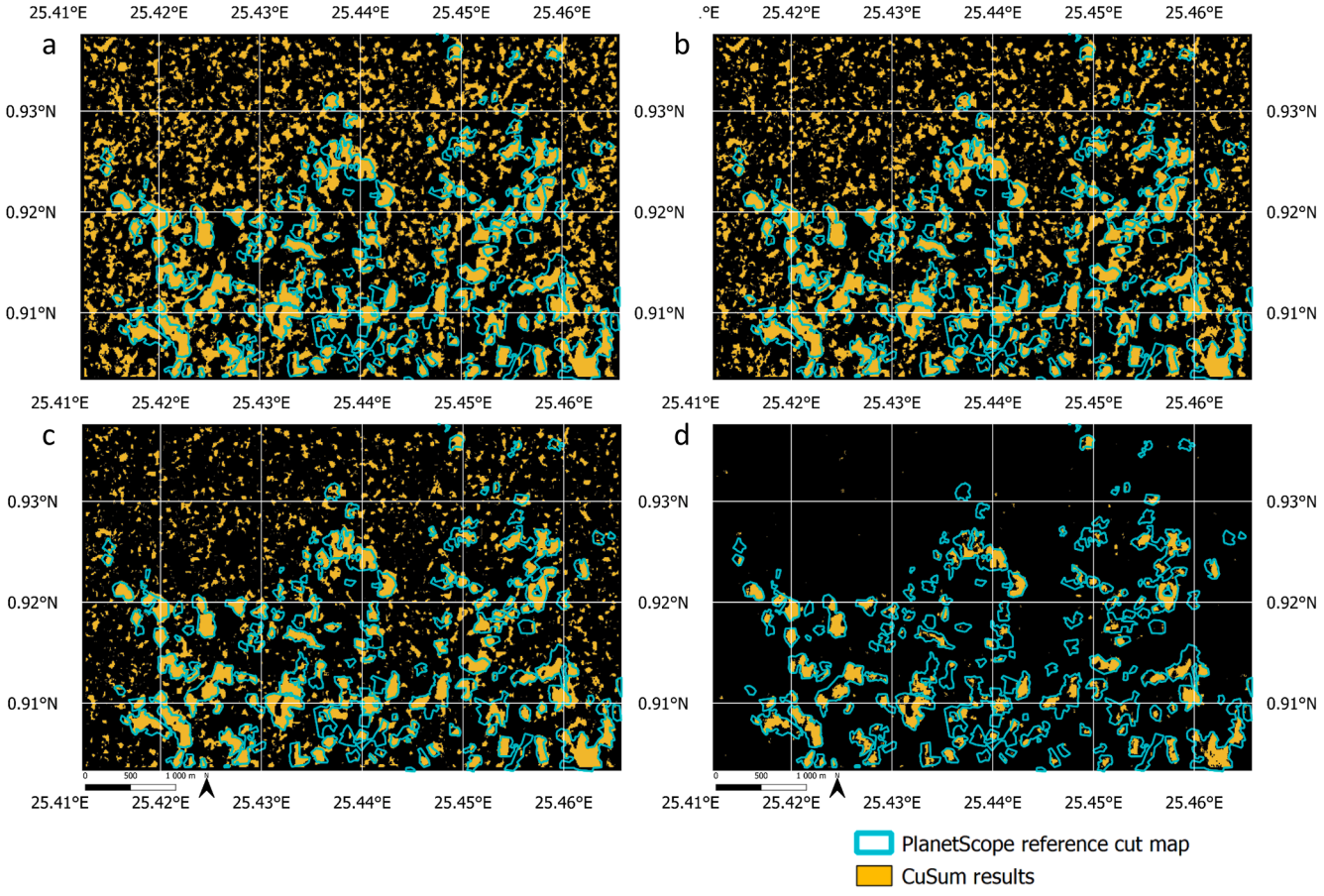

Fig. 7. CuSum algorithm results at VV polarization with T_c = (a) 0.25, (b) 0.50, (c) 0.75, (d) 1.00 with PlanetScope reference map cuts as blue-colored polygons. (For interpretation of the references to color in this figure legend, the reader is referred to the web version of this article.)

Table 3
Confusion matrix - derived statistics obtained by comparing the CuSum results to the PlanetScope reference map.

Base	T_c	Precision	Accuracy	Recall	Kappa coefficient	F1-score
VV	0.25	0.32	0.73	0.68	0.29	0.44
	0.50	0.35	0.77	0.67	0.33	0.46
	0.75	0.44	0.82	0.64	0.42	0.52
	1.00	0.87	0.90	0.40	0.50	0.55
	100_25	0.53	0.86	0.64	0.50	0.58
	100_50	0.59	0.88	0.64	0.54	0.61
	100_75	0.67	0.89	0.61	0.57	0.64
VH	0.25	0.23	0.57	0.76	0.15	0.35
	0.50	0.26	0.64	0.74	0.21	0.38
	0.75	0.34	0.75	0.70	0.32	0.46
	1.00	0.86	0.89	0.38	0.47	0.53
	100_25	0.25	0.63	0.76	0.20	0.38
	100_50	0.37	0.77	0.73	0.36	0.49
	100_75	0.54	0.86	0.68	0.52	0.60
VV union VH	0.25	0.21	0.50	0.80	0.11	0.33
	0.50	0.23	0.57	0.79	0.16	0.36
	0.75	0.29	0.69	0.76	0.26	0.42
	1.00	0.83	0.91	0.47	0.55	0.60
	100_25	0.21	0.52	0.80	0.12	0.33
	100_50	0.29	0.68	0.78	0.26	0.42
	100_75	0.46	0.83	0.74	0.47	0.57
VV intersect VH	0.25	0.41	0.81	0.64	0.39	0.50
	0.50	0.48	0.84	0.62	0.45	0.54
	0.75	0.63	0.88	0.58	0.54	0.60
	1.00	0.93	0.89	0.31	0.42	0.47
	100_25	0.65	0.89	0.59	0.55	0.62
	100_50	0.70	0.90	0.57	0.57	0.63
	100_75	0.77	0.91	0.55	0.59	0.64
legend	0 – 0.25	0.25 – 0.50	0.50 – 0.75	0.75 - 1		

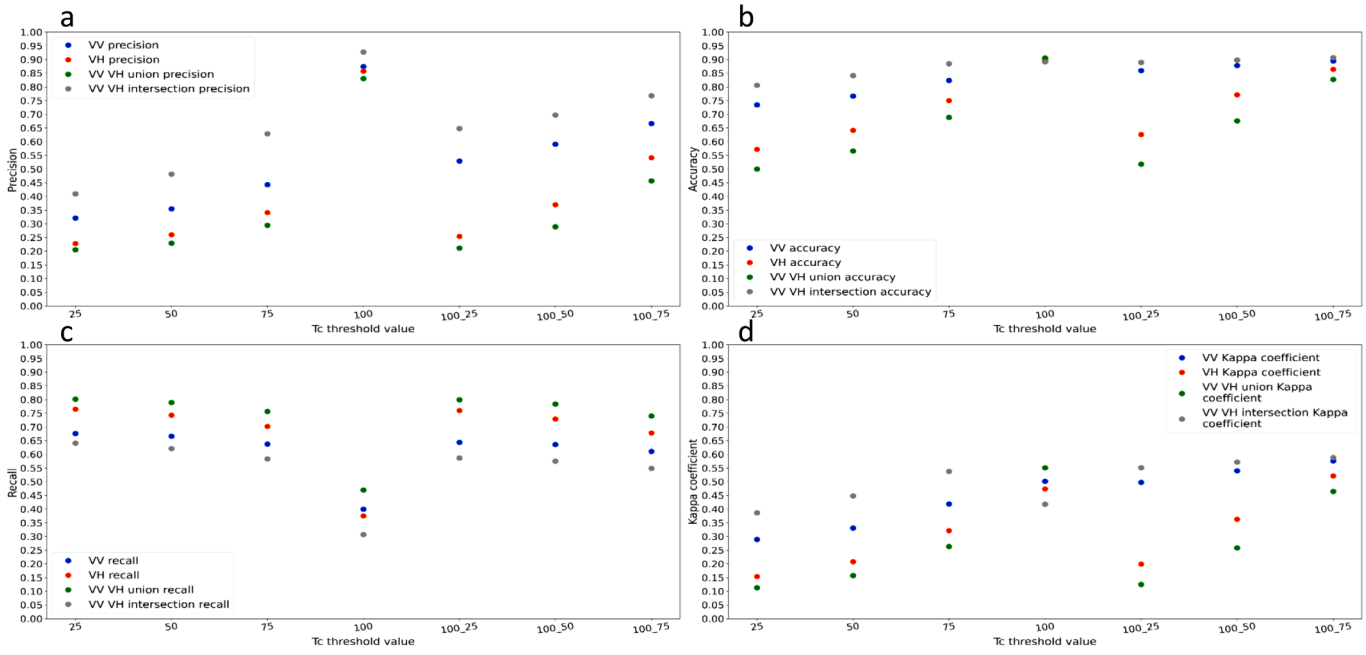

Fig. 8. CuSum results statistics based on Planet cut map of reference. (a) Precision, (b) Accuracy, (c) Recall, (d) Kappa coefficient.

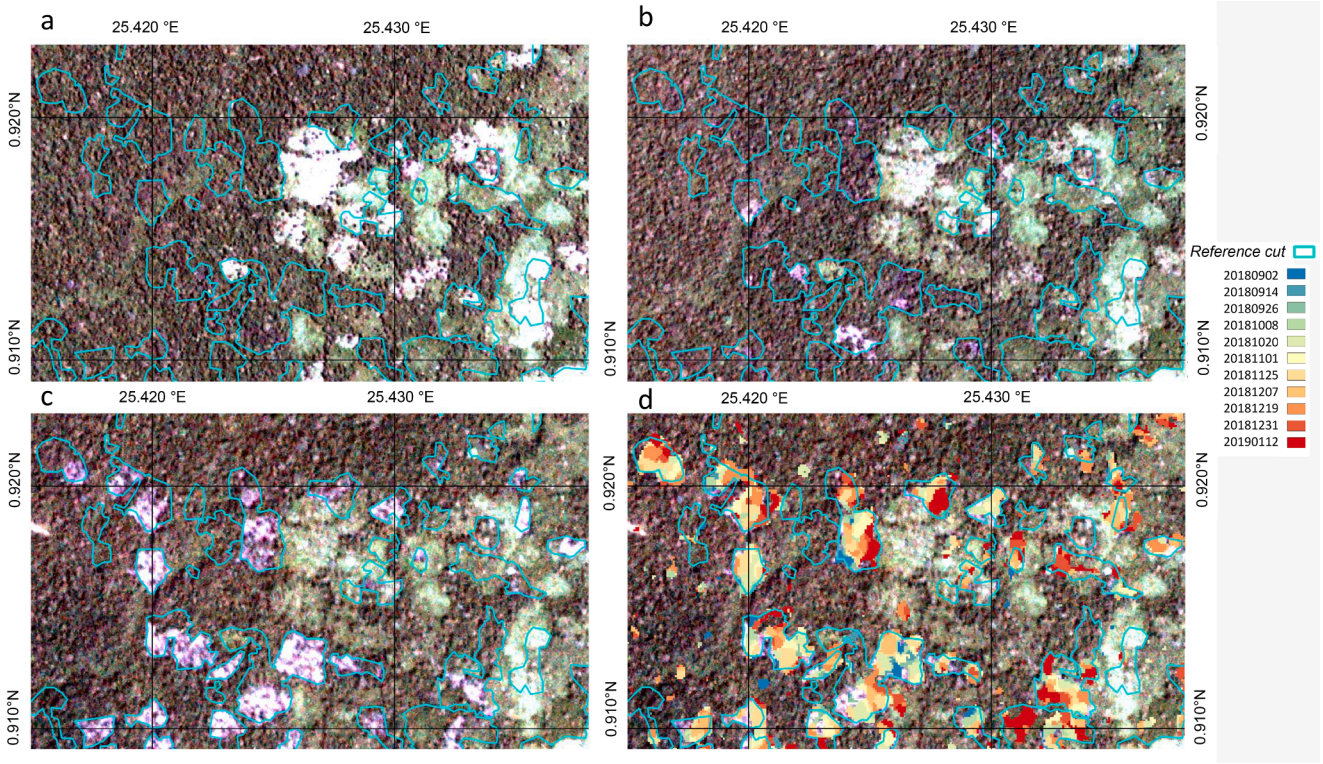

Fig. 9. (a) 10/09/2018 PlanetScope image, (b) 08/11/2018 PlanetScope image, (c) 03/01/2019 PlanetScope image, (d) CuSum results based on VV with $T_c = 0.75$. Blue polygons correspond to PlanetScope cut map. (For interpretation of the references to color in this figure legend, the reader is referred to the web version of this article.)

visually seen as deforested. The PlanetScope images exhibited a change in radiance in these zones but this change is much lower than that due to clear-cut. Later on (from a few days to 3 weeks later generally), most of these zones were cut. We assumed that the change in radiance in the PlanetScope images corresponds to degradation prior to deforestation. As the PlanetScope reference map we made does not consider "degradation" but only "deforestation", the value of the Kappa coefficient and precision may be impacted by the "degradation" events detected by CuSum but unconsidered by the reference map, thus remaining relatively low in comparison to the other (recall, accuracy) criteria.

According to the results some changes are well detected from only one polarization configuration (either VV or VH). This means both polarizations are affected differently by changes. But, overall, most big clusters of deforestation (showing a wide area labelled as deforestation on the reference map) are detected from both polarizations. The detection of a change by a polarization seems to be affected by (1) the nature of the change and (2) the magnitude of the change.

CuSum detected changes in many zones before their estimated dates of cut (64%, 167.3 ha, Table 4, Annex 1). This is consistent with the detection of degradations which occur before the reference dates of cut. Due to the relatively low availability of non-cloud-contaminated Planet images and the difficulty to monitor all degradations using this source, a precise estimate of the time-lag between degradation and cut could not be evaluated in this study, so that any change corresponding to a cut detected between the two nearest PlanetScope images is considered as a good detection.

Using two PlanetScope images separated by a long period would be suboptimal. Indeed, both degradation resulting in canopy gaps and canopy recovery may happen during a long period and the PlanetScope visual interpretation would then miss the degradation events that happened during that period. The use of a PlanetScope image temporally too close to the forest change detected by applying CuSum to Sentinel-1 SAR images can also miss the change. Indeed, this image may not be able to detect the forest degradation that was detected on the SAR images (as this change may not affect the canopy enough to be visible on the image). In both cases (small degradation and recovery), changes detected by the SAR images may not be detected by the Planet images. This effect may explain some false positives.

Note that the date pre-emptively detected is mostly detected within two weeks before the actual dates of cut. Nearly no detection of cuts was made later than the dates of cut seen through PlanetScope visual interpretation (5.93 % of the study area, corresponding to 15.49 ha), suggesting that some of the false positives made by applying CuSum are mainly due to degradation just before forest cut, and not by false detection of cut forests. Recent studies using Sentinel-1 images found that tropical canopy gaps and degraded canopy can be partially monitored using High Resolution SAR images (Numbisi and Van Coillie, 2020; Reiche et al., 2021). It seems that our results confirm these findings over our study area.

The sensitivity threshold (T_c) plays a crucial role for the precision and recall criteria of the algorithm. A high T_c value provides a robust result with many false negatives and very few false positives whereas a

Table 4
Temporal evaluation of the CuSum results based on VV with $T_c = 0.25$.

Time period monitored	Total TP Cut area (m^2)	TP change area detected in time (m^2)	TP change area detected early (m^2)	TP change area detected early (%)	TP change area detected late (m^2)	TP change area detected late (%)
2018/01/06–2019/11/26	2,613,700	782,500	1,676,300	64.14%	154,900	5.93%

low T_c value provides results reducing vastly the false negatives but greatly increasing the false positives. The combination of the results based on VV and VH and the use of cross-threshold T_c values seems to be a good compromise to optimize both accuracy and precision. The number of false positives is relatively large for all configurations, but as explained earlier, the reference map is not ground truth as no in-situ data was available and it did not account for forest degradation before forest cut. Despite this lack of in situ data, spatially & temporally consistent results were obtained in this study, making us confident in our evaluation. For instance, a spatial coherence of the cross-threshold results was found (Fig. 10): it seems the detected cuts form clusters which are dis-connected for high T_c values and the connection between clusters increase for decreasing T_c values, which could be interpreted by the fact roads or forest paths make connection between the different clusters of cut forests. It seems that small areas detected with a low T_c threshold and which are disconnected from the big clusters disappear for higher T_c values and are less reliable than those estimated with the "cross-threshold" clusters. The generalisation of this algorithm to dry forests and deciduous forest showing strong seasonal variability needs to be further tested, and the method probably adapted, as in Ruiz-Ramos et al., 2020.

6. Conclusion

Cover change in tropical forests is difficult to monitor due to the lack of in-situ data and the large-scale extent of deforestation. Using Sentinel-1C-SAR dual polarisation images, we were able to monitor cover changes in a Democratic Republic of Congo forest concession applying the CuSum approach to the Sentinel-1 SAR images.

According to accuracy assessment derived from the confusion matrix, CuSum applied to VV polarisation Sentinel-1 SAR images provides better results than using the VH polarization in terms of accuracy (minimal difference between VV and VH results of 1% for $T_c = 1.00$ up to 16% for $T_c = 0.25$), precision (minimal difference between VV and VH results of 0.01 for $T_c = 1.00$ up to 0.28 for 100_25) and Kappa coefficient (minimal difference between VV and VH results of 0.03 for $T_c = 1.00$ up to 0.30 for 100_25). The highest precision, related to the lowest False Negative ratio, was obtained using the intersection of VV with VH, with a minimal difference of 0.06 when comparing VV intersect VH $T_c = 1.00$ with VV $T_c = 1.00$ and a maximal difference of 0.33 when comparing VV intersect VH 100_50 with VH 100_50.

It is important to note that large differences of forest cut were found between our reference map based on PlanetScope (341.5 ha) and the GWF Cover Loss map (204 ha) in this area. It is probably due to the fact the tropical forest of DRC is often affected by cloud cover, and the better revisit time and resolution provided by PlanetScope OrthoScene led to improved detections. Our approach based on Sentinel-1 images is less affected by cloud cover, and the 12-day revisit time allows a good temporal monitoring. GFW Cover Loss map presents lower accuracy, precision, recall and kappa coefficient than the modified CuSum algorithm with a cross-Tc of 100_50. It also detects less true change area (189 ha) than the modified CuSum algorithm (up to 231.6 ha for VH 100_75).

The combination of the algorithm presenting the least false positives (high T_c value) with algorithms presenting more false positives (low T_c value) contributes to reduce the false positive errors obtained for low T_c values (minimum difference of 60.9 ha when comparing VV intersect VH $T_c = 0.75$ to VV intersect VH 100_75 to a maximum difference of 297.2 ha when comparing VH $T_c = 0.5$ to VH 100_50). It also contributes to reduce the false negative errors obtained for high T_c value (minimum

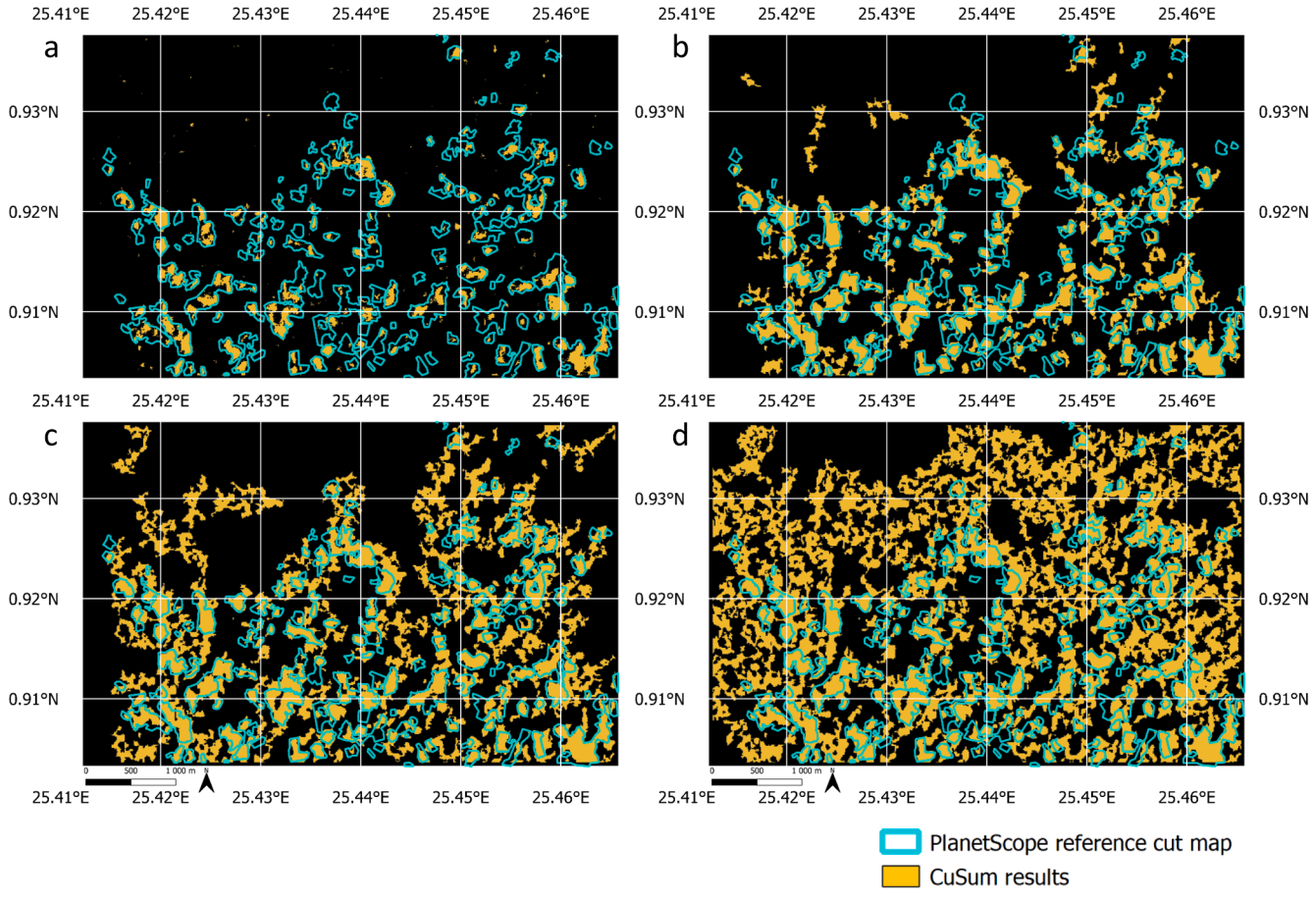

Fig. 10. Map of the CuSum spatial results for VH with (a) simple $T_c = 100$, (b) cross $T_c = 100$ and 75, (c) cross $T_c = 100$ and 50, (d) cross $T_c = 100$ and 25.

difference of 72 ha when comparing VV $T_c = 1.00$ to VV 100_75 to a maximum difference of 131.4 ha when comparing VH $T_c = 1.00$ to VH 100_25). Overall, the CuSum parameters that provided the best detection of vegetation cover change amongst the different polarisations and T_c configurations is VV intersect VH, cross-Tc 100_75 (Kappa coefficient: 0.59, Precision: 0.77, Accuracy: 0.91, Recall: 0.55).

The lack of in-situ data led us to use a PlanetScope-based reference map of the cover changes which is only based on remotely sensed optical observations and which present many limitations. In particular, degradation effects preceding deforestation were not monitored in this reference map, and canopy gaps can recover between two images. This could partially explain why our results, based on Sentinel-1 SAR images, exhibit more changes than detected in the reference map. This could also explain the lower scores obtained at VH than at VV when applying CuSum to Sentinel-1 images as observations at the VH polarisation are more sensitive to the degradation effects than at the VV polarisation (Kellndorfer, 2019). This could affect the false positives detected using VH: they are more numerous compared to using VV. In conclusion, some of the false positives can be attributed to degradation detected using Sentinel-1 SAR images that cannot be identified using optical images as previously noted by Numbisi and van Collie (2020) and Reiche et al. (2021).

The major drawback of our approach is its limitation to the detection of only one change against time. Once a pixel is affected by a change, its status does not evolve against time. We are currently working on a multi-temporal detection change approach that will be helpful to characterize the evolution of the forest cover from degradation to deforestation and then the possible recovery and could also be applied for the monitoring of lower vegetation canopy types.

Declaration of Competing Interest

The authors declare that they have no known competing financial interests or personal relationships that could have appeared to influence the work reported in this paper.

Acknowledgements

This work was supported by VisioTerra. We also thank the reviewers for helping us improving the manuscript.

Appendix A

Annexe 1: Table of the detection time of the change.

Time period monitored	Cut area (m^2)	Change area detected in time (m^2)	Change area detected early (m^2)	Change area detected early (%)	Change area detected late (m^2)	Change area detected late (%)
2018/01/06–2018/02/02	52,700	22,100	0	0.00%	30,600	58.06%
2018/02/02–2018/03/17	56,700	30,000	4400	7.76%	22,300	39.33%
2018/03/17–2018/04/19	5600	800	3000	53.57%	1800	32.14%
2018/04/19–2018/06/15	29,400	23,300	1900	6.46%	4200	14.29%
2018/06/15–2018/08/17	18,200	13,000	2700	14.84%	2500	13.74%
2018/08/17–2018/09/10	3400	0	1500	44.12%	1900	55.88%
2018/09/10–2018/11/08	110,700	60,500	22,400	20.23%	27,800	25.11%
2018/11/08–2018/12/19	565,400	214,300	324,100	57.32%	27,000	4.78%
2018/12/19–2019/01/06	386,000	143,300	229,500	59.46%	13,200	3.42%
2019/01/06–2019/01/22	359,200	88,500	260,300	72.47%	10,400	2.90%
2019/01/22–2019/02/02	193,200	24,100	163,500	84.63%	5600	2.90%
2019/02/02–2019/03/03	484,400	93,600	384,800	79.44%	6000	1.24%
2019/03/03–2019/03/31	108,900	11,000	97,500	89.53%	400	0.37%
2019/03/31–2019/05/03	11,100	100	10,200	91.89%	800	7.21%
2019/05/03–2019/08/06	70,600	23,100	47,100	66.71%	400	0.57%
2019/08/06–2019/11/10	46,200	28,700	17,500	37.88%	0	0.00%
2019/11/10–2019/11/26	112,000	6100	105,900	94.55%	0	0.00%
Total	2,613,700	782,500	1,676,300	64.14%	154,900	5.93%

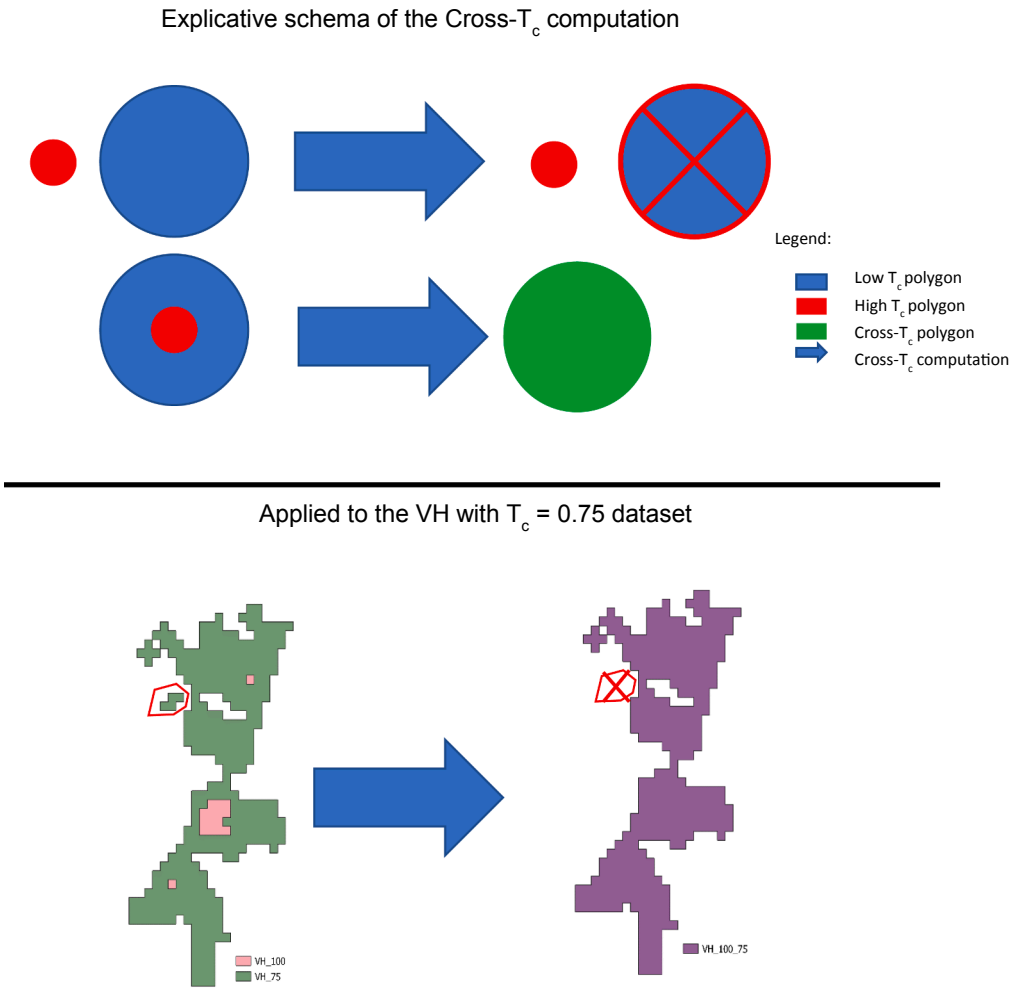

Annexe 2: Supplementary material: explicative schema of the Cross-T_c computation.

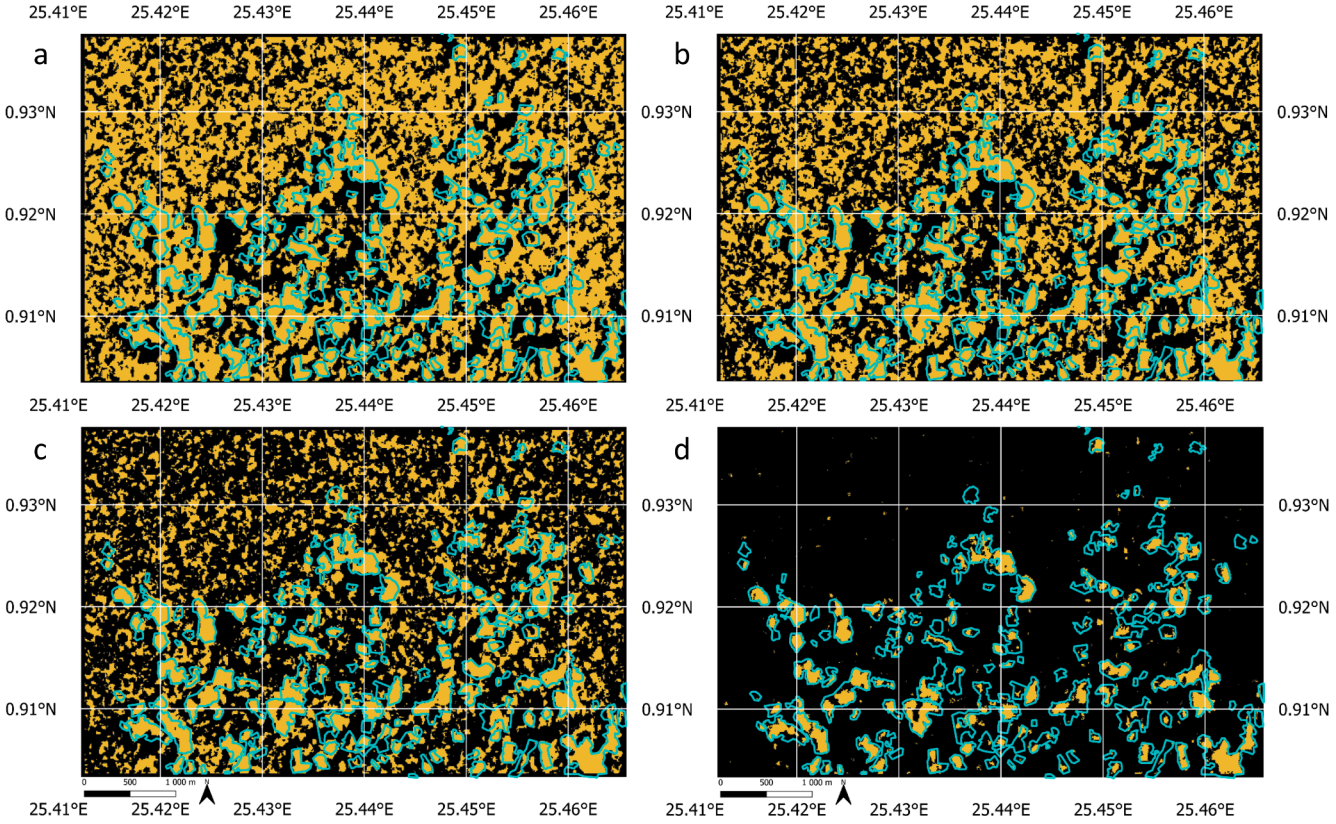

Annexe 3: Map of the results of the CuSum based on VV union VH with T_c = (a) 0.25, (b) 0.50, (c) 0.75 et (d) 1.00.

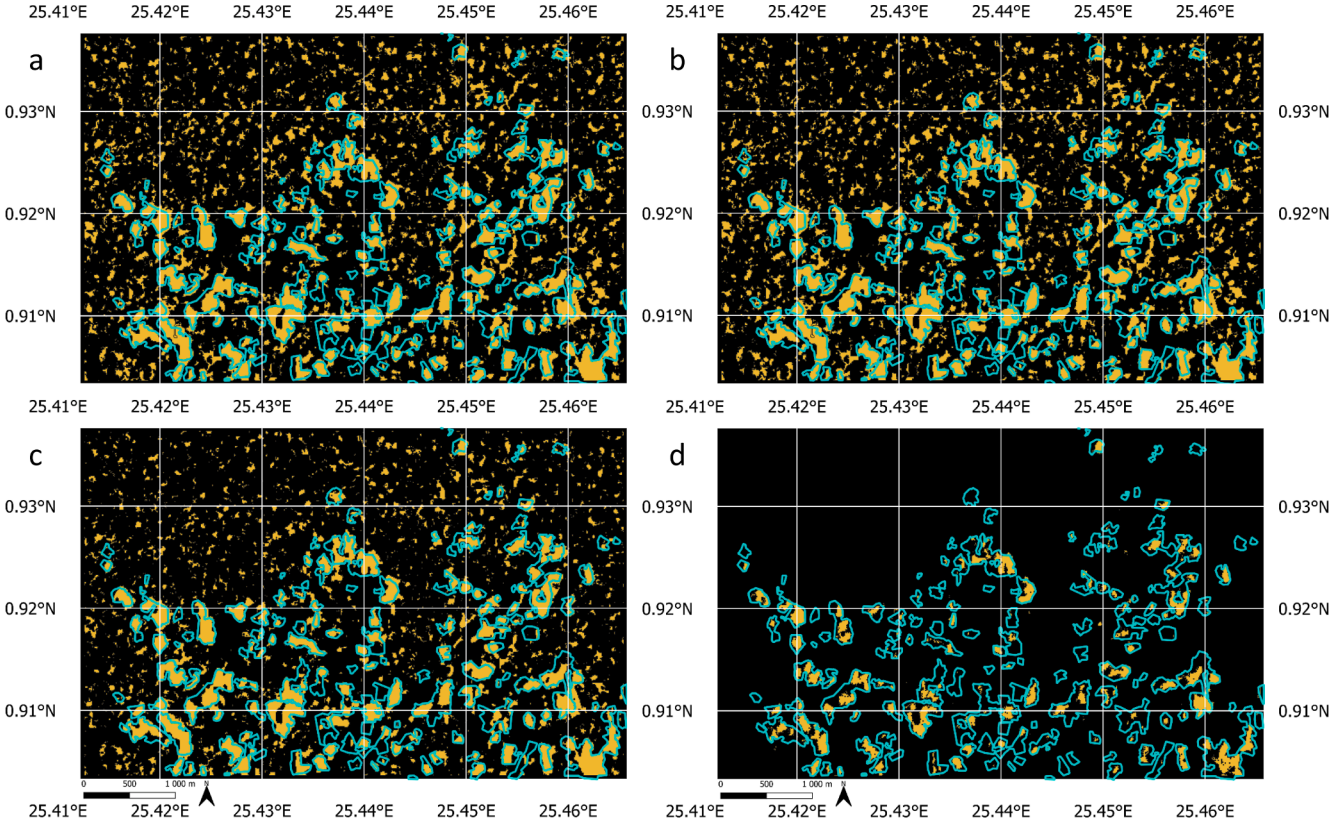

Annexe 5: Map of the results of the CuSum based on VV intersect VH with (a) Tc = 1.00, (b) cross-T_c 100_75, (c) cross-T_c 100_50 and (d) cross-T_c 100_25.

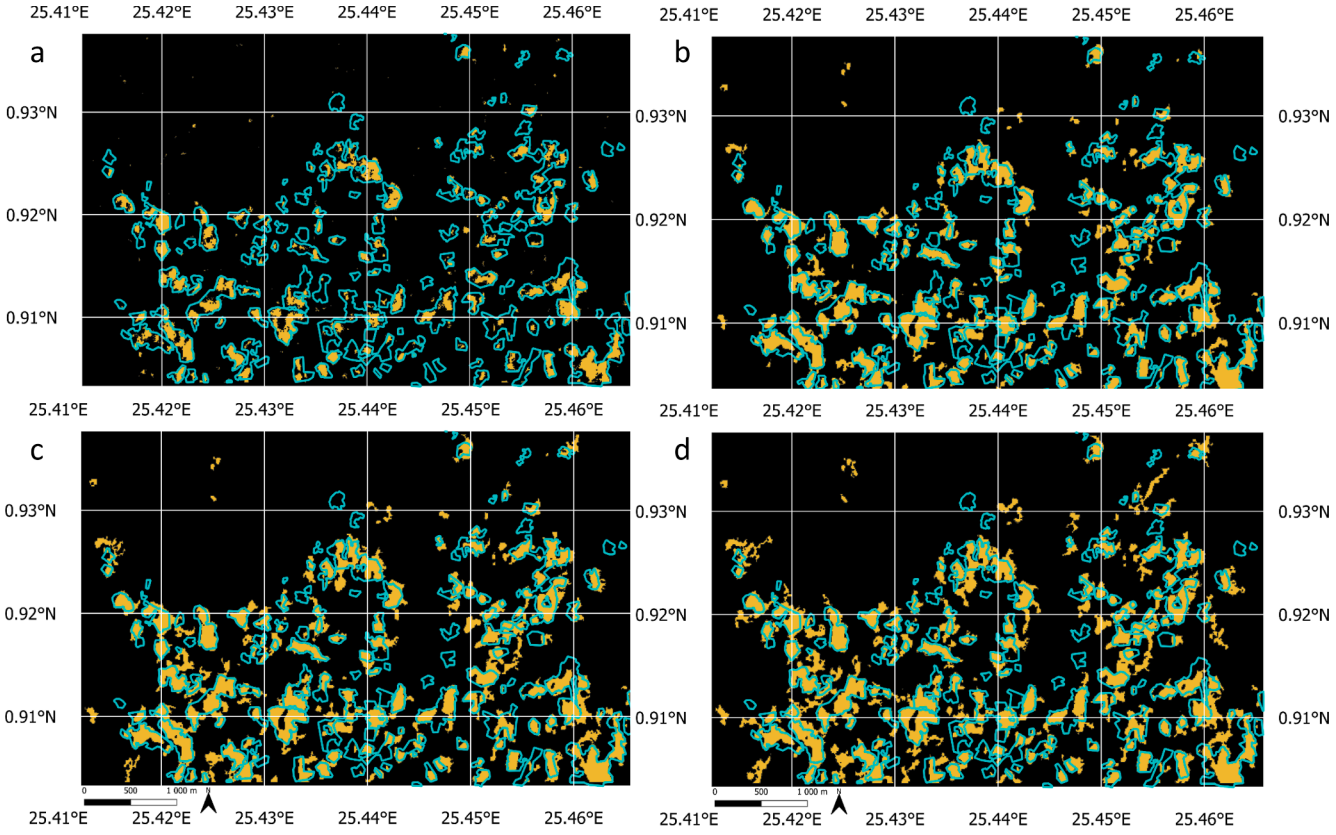

Annexe 4: Map of the results of the CuSum based on VV intersect VH with T_c = (a) 0.25, (b) 0.50, (c) 0.75 et (d) 1.00.

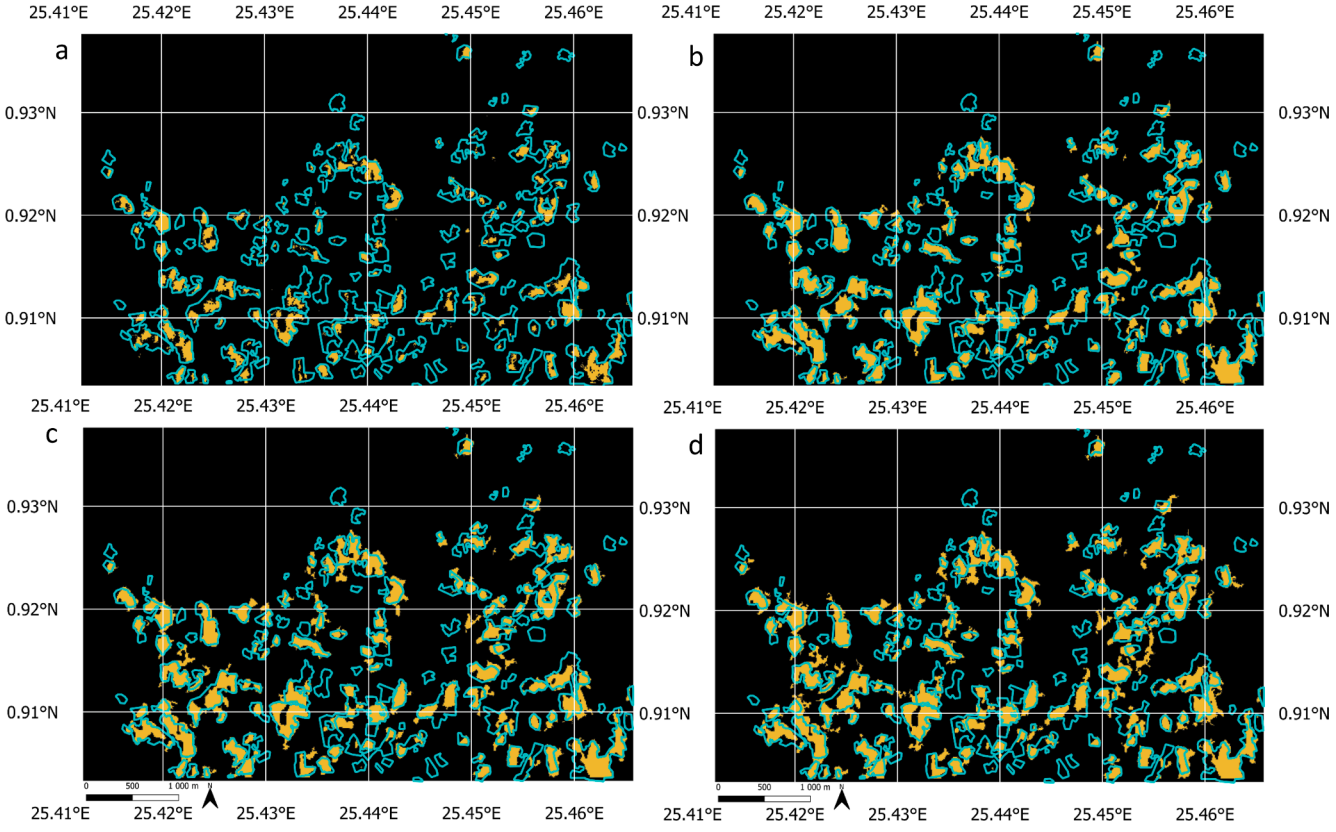

Annexe 6: Map of the results of the CuSum based on VV intersect VH with (a) $T_c = 1.00$, (b) cross-T_c 100_75, (c) cross-T_c 100_50 and (d) cross-T_c 100_25.

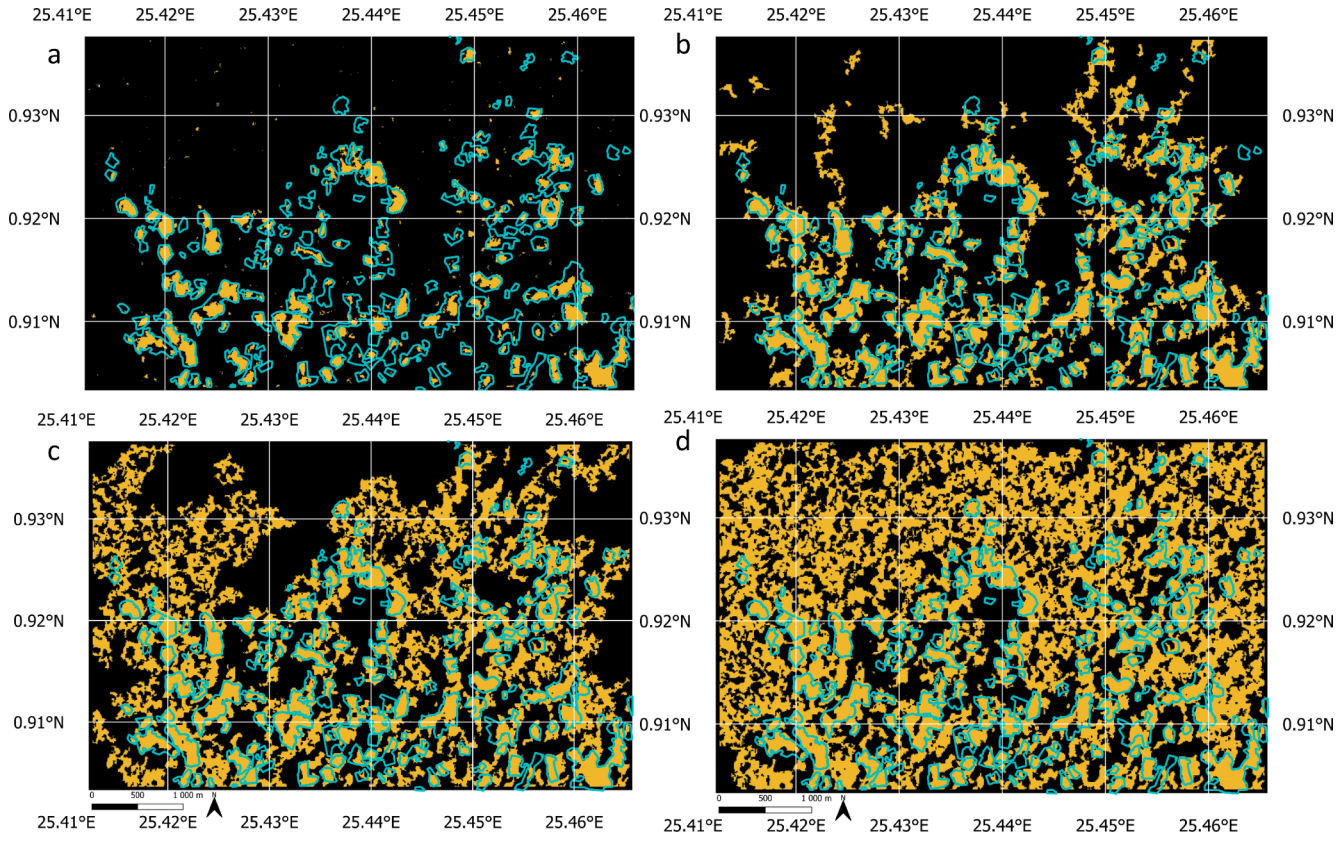

Annexe 7: Map of the results of the CuSum based on VV union VH with (a) $T_c = 1.00$, (b) cross-T_c 100_75, (c) cross-T_c 100_50 and (d) cross-T_c 100_25.

References

W. Alpers, C. Melsheimer, Rainfall. Synth. Aperture Radar Mar. user's Man; 2004. p. 355–371.

Antropov, O., Rauste, Y., Väänänen, A., Mutanen, T., Häme, T., 2016. Mapping forest disturbance using long time series of Sentinel-1 data: Case studies over boreal and tropical forests. In: 2016 IEEE International Geoscience and Remote Sensing Symposium (IGARSS), pp. 3906–3909. https://doi.org/10.1109/IGARSS.2016.7730014.

Belenguer-Plomer, M.A., Chuvieco, E., Tanase, M.A., 2019. Temporal decorrelation of c-band backscatter coefficient in mediterranean burned areas. Remote Sens. 11, 1–19. https://doi.org/10.3390/rs11222661.

Bouvet, A., Mermoz, S., Ballère, M., Koleck, T., Le Toan, T., 2018. Use of the SAR shadowing effect for deforestation detection with Sentinel-1 time series. Remote Sens. 10, 1–19. https://doi.org/10.3390/rs10081250.

Bullock, E.L., Woodcock, C.E., Souza Jr, C., Olofsson, P., 2020. Satellite-based estimates reveal widespread forest degradation in the Amazon. Glob. Chang. Biol. 26, 2956–2969.

Coelho, L.P., 2013. Mahotas: Open source software for scriptable computer vision. J. Open Res. Softw. 1, e3 https://doi.org/10.5334/jors.ac.

Contreras-Hermosilla, A., et al., 2000. The underlying causes of forest decline. JSTOR.

Duveiller, G., Defourny, P., Desclée, B., Mayaux, P., 2008. Deforestation in Central Africa: estimates at regional, national and landscape levels by advanced processing of systematically-distributed Landsat extracts. Remote Sens. Environ. 112, 1969–1981. https://doi.org/10.1016/j.rse.2007.07.026.

Federici, S., Tubiello, F.N., Salvatore, M., Jacobs, H., Schmidhuber, J., 2015. New estimates of CO2 forest emissions and removals: 1990–2015. For. Ecol. Manage. 352, 89–98. https://doi.org/10.1016/j.foreco.2015.04.022.

Hamunyela, E., Herold, M., Verbesselt, J., 2017. Space-time monitoring of tropical forest changes using observations from multiple satellites. Ph.D. Thesis, Wageningen University & Research, Laboratory of Geo-information Science and Remote Sensing, Wageningen, The Netherlands.

Hamunyela, E., Rosca, S., Mirt, A., Engle, E., Herold, M., Gieseke, F., Verbesselt, J., 2020. Implementation of BFASTmonitor Algorithm on Google Earth Engine to support large-area and sub-annual change monitoring using earth observation data. Remote Sens. 12 https://doi.org/10.3390/RS12182953.

Hamunyela, E., Verbesselt, J., Herold, M., 2016. Using spatial context to improve early detection of deforestation from Landsat time series. Remote Sens. Environ. 172, 126–138. https://doi.org/10.1016/j.rse.2015.11.006.

Hansen, M.C., Krylov, A., Tyukavina, A., Potapov, P.V., Turubanova, S., Zutta, B., Ifo, S., Margono, B., Stolle, F., Moore, R., 2016. Humid tropical forest disturbance alerts using Landsat data. Environ. Res. Lett. 11 https://doi.org/10.1088/1748-9326/11/3/034008.

Hansen, M.C., Potapov, P. V., Moore, R., Hancher, M., Turubanova, S.A., Tyukavina, A., Thau, D., Stehman, S. V., Goetz, S.J., Loveland, T.R., Kommareddy, A., Egorov, A., Chini, L., Justice, C.O., Townshend, J.R.G., 2013. High-resolution global maps of 21st-century forest cover change. Science (80-.). 342, 850–853. https://doi.org/10.1126/science.1244693.

Haralick, R.M., Shanmugam, K., Dinstein, I.H., 1973. Textural features for image classification. IEEE Trans. Syst. Man. Cybern. 610–621.

Joshi, N., Mitchard, E.T.A., Woo, N., Torres, J., Moll-Rocek, J., Ehammer, A., Collins, M., Jepsen, M.R., Fensholt, R., 2015. Mapping dynamics of deforestation and forest degradation in tropical forests using radar satellite data. Environ. Res. Lett. 10 https://doi.org/10.1088/1748-9326/10/3/034014.

Kellndorfer, J., 2019. Using SAR data for mapping deforestation and forest degradation, in: THE SAR HANDBOOK Comprehensive Methodologies for Forest Monitoring and Biomass Estimation. ServirGlobal : Huntsville, AL, pp. 65–79.

Kucera, J., Barbosa, P., Strobl, P., 2007. Cumulative Sum Charts - A Novel Technique for Processing Daily Time Series of MODIS Data for Burnt Area Mapping in Portugal. In: 2007 International Workshop on the Analysis of Multi-Temporal Remote Sensing Images, pp. 1–6. https://doi.org/10.1109/MULTITEMP.2007.4293051.

Lievens, H., Martens, B., Verhoest, N.E.C., Hahn, S., Reichle, R.H., Miralles, D.G., 2017. Assimilation of global radar backscatter and radiometer brightness temperature

observations to improve soil moisture and land evaporation estimates. Remote Sens. Environ. 189, 194–210. https://doi.org/10.1016/j.rse.2016.11.022.
Manogaran, G., Lopez, D., 2018. Spatial cumulative sum algorithm with big data analytics for climate change detection. Comput. Electr. Eng. 65, 207–221. https://doi.org/10.1016/j.compeleceng.2017.04.006.
Numbisi, F.N., Van Coillie, F., 2020. Does sentinel-1A backscatter capture the spatial variability in canopy gaps of tropical agroforests? A proof-of-concept in cocoa landscapes in Cameroon. Remote Sens. 12, 1–29. https://doi.org/10.3390/rs12244163.
Nunes, L.J.R., Meireles, C.I.R., Gomes, C.J.P., Ribeiro, N.M.C.A., 2020. Forest contribution to climate change mitigation: Management oriented to carbon capture and storage. Climate 8. https://doi.org/10.3390/cli8020021.
Olofsson, P., Foody, G.M., Herold, M., Stehman, S.V., Woodcock, C.E., Wulder, M.A., 2014. Good practices for estimating area and assessing accuracy of land change. Remote Sens. Environ. 148, 42–57. https://doi.org/10.1016/j.rse.2014.02.015.
Piantanida, R., Miranda, N., 2017. Thermal Denoising of Products Generated by the S-1 IPF.
Potapov, P., Hansen, M.C., Kommareddy, I., Kommareddy, A., Turubanova, S., Pickens, A., Adusei, B., Tyukavina, A., Ying, Q., 2020. Landsat analysis ready data for global land cover and land cover change mapping. Remote Sens. 12 https://doi.org/10.3390/rs12030426.
Reiche, J., Hamunyela, E., Verbesselt, J., Hoekman, D., Herold, M., 2018a. Improving near-real time deforestation monitoring in tropical dry forests by combining dense Sentinel-1 time series with Landsat and ALOS-2 PALSAR-2. Remote Sens. Environ. 204, 147–161. https://doi.org/10.1016/j.rse.2017.10.034.
Reiche, J., Mullissa, A., Slagter, B., Gou, Y., Tsendbazar, N.-E., Odongo-Braun, C., Vollrath, A., Weisse, M.J., Stolle, F., Pickens, A., Donchyts, G., Clinton, N., Gorelick, N., Herold, M., 2021. Forest disturbance alerts for the Congo Basin using Sentinel-1. Environ. Res. Lett. 16, 024005 https://doi.org/10.1088/1748-9326/abd0a8.
Reiche, J., Verhoeven, R., Verbesselt, J., Hamunyela, E., Wielaard, N., Herold, M., 2018b. Characterizing tropical forest cover loss using dense Sentinel-1 data and active fire alerts. Remote Sens. 10, 1–18. https://doi.org/10.3390/rs10050777.
Reigber, A., del Campo Becerra, G.M., Jäger, M., 2019. PyRAT: A Flexible SAR Postprocessing Toolbox, in: ESA POLinSAR Workshop.
Rüetschi, M., Small, D., Waser, L.T., 2019. Rapid detection of windthrows using Sentinel-1 C-band SAR data. Remote Sens. 11, 1–23. https://doi.org/10.3390/rs11020115.
Ruiz-Ramos, J., Marino, A., Boardman, C., Suarez, J., 2020. Continuous forest monitoring using cumulative sums of sentinel-1 timeseries. Remote Sens. 12 https://doi.org/10.3390/RS12183061.
Ruiz-ramos, J., Marino, A., Boardman, C.P., 2018. USING SENTINEL 1-SAR FOR MONITORING LONG TERM VARIATION IN BURNT FOREST AREAS Javier Ruiz-Ramos ; Armando Marino ; Carl P . Boardman. IGARSS 2018 - 2018 IEEE Int. Geosci. Remote Sens. Symp. 4901–4904.
Small, D., 2011. Flattening gamma: Radiometric terrain correction for SAR imagery. IEEE Trans. Geosci. Remote Sens. 49, 3081–3093. https://doi.org/10.1109/TGRS.2011.2120616.
Souza, C.M., Siqueira, J.V., Sales, M.H., Fonseca, A.V., Ribeiro, J.G., Numata, I., Cochrane, M.A., Barber, C.P., Roberts, D.A., Barlow, J., 2013. Ten-year landsat classification of deforestation and forest degradation in the Brazilian amazon. Remote Sens. 5, 5493–5513. https://doi.org/10.3390/rs5115493.
Takeuchi, S., Suga, Y., Yoshimura, M., 2001. A comparative study of coherence information by L-band and C-band SAR for detecting deforestation in tropical rain forest, in: IGARSS 2001. Scanning the Present and Resolving the Future. Proceedings. IEEE 2001 International Geoscience and Remote Sensing Symposium (Cat. No.01CH37217). pp. 2259–2261 vol.5. https://doi.org/10.1109/IGARSS.2001.977968.
Tanase, M.A., Kennedy, R., Aponte, C., 2015. Radar Burn Ratio for fire severity estimation at canopy level: an example for temperate forests. Remote Sens. Environ. 170, 14–31. https://doi.org/10.1016/j.rse.2015.08.025.
Tanase, M.A., Perez-Cabello, F., de la Riva, J., Santoro, M., 2010. TerraSAR-X data for burn severity evaluation in mediterranean forests on sloped terrain. IEEE Trans. Geosci. Remote Sens. 48, 917–929. https://doi.org/10.1109/TGRS.2009.2025943.
Tomasi, C., Manduchi, R., 1998. Bilateral filtering for gray and color images. Proc. IEEE Int. Conf. Comput. Vis. 839–846 https://doi.org/10.1109/iccv.1998.710815.
Tyukavina, A., Hansen, M.C., Potapov, P., Parker, D., Okpa, C., Stehman, S.V., Kommareddy, I., Turubanova, S., 2018. Congo Basin forest loss dominated by increasing smallholder clearing. Sci. Adv. 4 https://doi.org/10.1126/sciadv.aat2993.
Watanabe, M., Koyama, C.N., Hayashi, M., Nagatani, I., Shimada, M., 2018. Early-stage deforestation detection in the tropics with L-band SAR. IEEE J. Sel. Top. Appl. Earth Obs. Remote Sens. 11, 2127–2133. https://doi.org/10.1109/JSTARS.2018.2810857.
Watanabe, M., Koyama, C.N., Hayashi, M., Nagatani, I., Tadono, T., Shimada, M., 2021. Refined algorithm for forest early warning system with ALOS-2/PALSAR-2 ScanSAR data in tropical forest regions. Remote Sens. Environ. 265, 112643 https://doi.org/10.1016/j.rse.2021.112643.
Whittle, M., Quegan, S., Uryu, Y., Stüewe, M., Yulianto, K., 2012. Detection of tropical deforestation using ALOS-PALSAR: A Sumatran case study. Remote Sens. Environ. 124, 83–98. https://doi.org/10.1016/j.rse.2012.04.027.
COD Forest Atlas, 2016. https://cod.forest-atlas.org/ accessed December, 2019.
COPERNICUS, 2015. accessed January, 2020.
Global Forest Watch, 2015. https://data.globalforestwatch.org/ accessed March, 2020.
Planet, 1996. https://www.planet.com accessed June, 2020.
SAR Users Manuals from NOAA, http://ww.w.sarusersmanual.com accessed June, 2021.
VtWeb, 2015. https://visioterra.org/VtWeb/ accessed November, 2020.
JJ-FAST, http://www.eorc.jaxa.jp/jjfast/jj_index.html, Accessed June 16, 2021.